Acoustoelectric Current in Suspended Quantum Point Contacts

By

Dustin J. Kreft

A dissertation submitted in partial fulfillment of

the requirements for the degree of

Doctor of Philosophy

(Electrical Engineering)

at the

UNIVERSITY OF WISCONSIN-MADISON

2012

Date of final oral examination: 5/4/2012

The dissertation is approved by the following members of the Final Oral Committee:

Robert H. Blick, Professor, Electrical Engineering
Zhenqiang (Jack) Ma, Professor, Electrical Engineering
Dan Botez, Professor, Electrical Engineering
Luke Mawst, Professor, Electrical Engineering
Maxim Vavilov, Assistant Professor, Physics

Table of Contents

Acknowledgements

I would like to thank Robert H. Blick, my professor and advisor, for allowing me the opportunity to be a part of his research team. His creativity and insight has made my Ph.D. work a challenge and a reward. I would like to give extended thanks for his guidance and patience through these years.

I would also like to thank the current and past group members for offering their knowledge and aid in assisting me in my research: Hyun Cheol Shin, Hyun Cheol (Caleb) Shin, Dr. Eric Stava, Dr. Jonghoo Park, Hyunseok Kim, Abhishek Bhat, Dr. Hua Qin, Sean O'Connor, and Dr. Chulki Kim.

I would like to thank God, through Him all things are possible; even the rigors of scientific research and success. For without Him we wouldn't have anything to study or understand.

List of Publications

[1] D.J. Kreft, L.G. Murokh, H.C. "Caleb" Shin, M. Bichler, W. Wegscheider, and R.H. Blick, *Giant Acoustoelectric Current in Suspended Quantum Point Contacts*, Phys. Rev. Lett., *in preparation*

[2] D.J. Kreft and R.H. Blick, *Surface Acoustic Waves and Nano-Electromechanical Systems, Acoustic Waves – From Microdevices to Helioseismology*, M.G. Beghi (Ed.), 2011, ISBN: 978-953-307-572-3, InTech

[3] A. Bhat, J. Rodriguez, H. Qin, H.C. Shin, H.C. "Caleb" Shin, D.J. Kreft, J. Park, E.J. Stava, M. Yu, and R.H. Blick, *Simulation and Measurement Analysis of a Radio Frequency Tank Circuit for Biological Probing*, *in preparation*

[4] S.H. Baek *et al.*, *Giant Piezoelectricity on Si for Hyperactive NEMS*, Science **334**, 598 (2011)

[5] M. Yu, H.C. Shin, E.J. Stava, D.J. Kreft, and R.H. Blick, *Microfabrication and Dynamic Tuning of Small and Smooth Pores in Crystalline Quartz*, Biosensors and Bioelectronics, 2011, *submitted*

List of Figures

CHAPTER 1

◄ Introduction ►

1.1 Motivation

The motivations for this research are several. As current devices are becoming smaller the general trend of research is to probe into the known and unknown quantum effects to further the understanding required to push everyday technology into another era of smaller, faster, and more efficient. This is easily realized in the area of semiconductor physics in the industrial realm of the metal-oxide-semiconductor field-effect-transistor (MOSFET). As these devices shrink to dimensions that approach the limit where quantum effects must now be considered in order to produce the next generation of microprocessor we need to further our research to continue next generation technology. The MOSFET is often cited as a reference point for most nano research since that technology has such a large impact as being the basis for computing and thinking devices, as of the time of this thesis.

As this thesis progresses you will see how the information contained here further expands upon nano electromechanical systems (NEMS) and micro electromechanical systems (MEMS). As this is the field of most interest to me in that it expounds upon a plethora of information and device structures for the purpose increasing knowledge in the

areas of electron-phonon interactions, mechanical interactions on electron systems, viewing quantum effects outside of the standard low temperature regime, and the challenge of it all.

One of the most sought after methods for solid state devices is to produce a quantized current standard for metrology. This has uses in testing devices as well as producing a single electron current source for quantum computing systems and other single electron transistor devices. For this reason surface acoustic waves (SAWs) have gained a lot of attention in low-dimensional systems. Research has been done to understand SAWs in many different environments. This research has aimed to offer a new approach to investigate SAWs. Here SAWs are transmitted into a suspended nano bridge which has five quantum point contacts (QPCs) patterned onto the surface. In this regime the effects are amplified which lead to some very interesting results.

On top of SAWs being currently used widely in the areas of RFID tags and delay lines for satellite receivers they still offer a look into the quantum world which will be seen through this thesis and, as a motivation, will offer some new insight into the world as they are used for low-dimensional systems.

1.1.1 Outline of Thesis

This thesis is laid out in the following fashion. Chapter 1 gives some of the basic background needed for understanding SAWs as they interact with 2DEGs along with

QPC information and behavior. Chapter 2 details the fabrication process for creating the devices used in the research discussed in this thesis. Chapter 3 gives a brief outline of the measurement equipment used. Chapters 4 and 5 give the results of the measurements as well as the theoretical details needed to interpret and understand the results. Chapter 5 focuses on the results that are still currently under investigation and will continue to be worked on after submission of this thesis.

The reader of this thesis may skip forward to Chapters 4 and 5 if they wish to focus more on the results and applied theory.

1.2 Introduction to Surface Acoustic Waves

A surface acoustic wave (SAW) is a Rayleigh wave which travels primarily along the surface of a material. This first occurs by introducing an electric field through the material by use of metallic electrodes, see Fig. 1.2.1a. As the electric field lines penetrate in to the piezoelectric material the material itself will start to deform in accordance with the inverse piezoelectric effect. This wave will then travel along the surface of the material causing a wave-like deformation, see Fig. 1.2.1.d. This deformation will drag electrons along with it through the traveling electric potential that is created, see Eq. 2.

The wave is elliptical in nature, see Fig. 1.2.1b, although it can be accurately described using a standard wave equation [1]. Equation 1 is used to describe the deformation of the surface as the wave travels. From here we will refer to Fig. 1.2.1c to identify the coordinates in relation to the equations and figures presented [2]. We see that from Eq. 1 the exponential y term shows a rapid wave decay as it penetrates the depth of the material. The wave is contained within one wavelength, λ, from the surface of the material. At a distance of λ from the surface the wave is nearly completely attenuated and does not penetrate further into the material. Equation 5 can be used to calculate the linear strain of the material from the SAW and then be used calculate the piezoelectrical mechanical stress which is shown in Eq. 4. As this wave travels along with it is a traveling electric potential, see Eq. 2, in which the electric field is given by Eq. 3 [1-2]. The electric field will be contained within the material except for a small fraction in

which the field lines will go beyond the surface and extend into free space [1]. Again, the induced electric potential will fully decay within one wavelength of the material surface. This traveling electric potential will cause a "deformation" in the valence and conduction energy bands of the material [3]. As this electric potential locally raises and lowers the Fermi energy it creates traps for majority carries, in this case electrons, and allows these carries to transfer into the wells of the potential [3], see Fig 1.2.2.

$$U = |U| e^{i(\omega t - kz)} e^{-k|y|} \tag{1}$$

$$\Phi = |\Phi| e^{i(\omega t - kz)} e^{-k|y|} \tag{2}$$

$$E_i = -\frac{\partial \Phi}{\partial x_i} \tag{3}$$

$$T_{ij} = c_{ijkl} S_{kl} + e_{nij} E_n \tag{4}$$

$$S_{kl} = \frac{1}{2}\frac{\partial u_k}{\partial x_l} + \frac{\partial u_l}{\partial x_k} \tag{5}$$

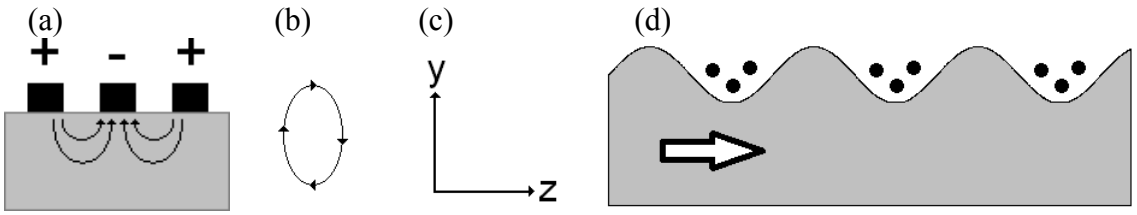

Fig. 1.2.1. (a) Electric field lines penetrating into the piezoelectric material which will cause deformation through the inverse piezoelectric effect. Black squares indicate metallic gates, see section 1.3. (b) Elliptical orbit of Rayleigh wave. (c) Axis of orientation in reference to the material when applied to the needed equations. (d) Deformation of surface showing a wave traveling in the direction indicated by the arrow. Black dots indicate electrons being trapped and mechanically transported across the material.

Once these electrons are contained they are mechanically moved along the direction of SAW propagation and thus create a direct current in the system despite the SAW being a traveling oscillating wave. The transfer of electrons creates a quantized current following

$$I = n\, e\, f \tag{6}$$

where e is the fundamental charge of an electron, f is the frequency of the SAW, and n is the number of electrons being transferred per cycle. This effect can be used to trap and hold excitons which can be later released to emit photons [4].

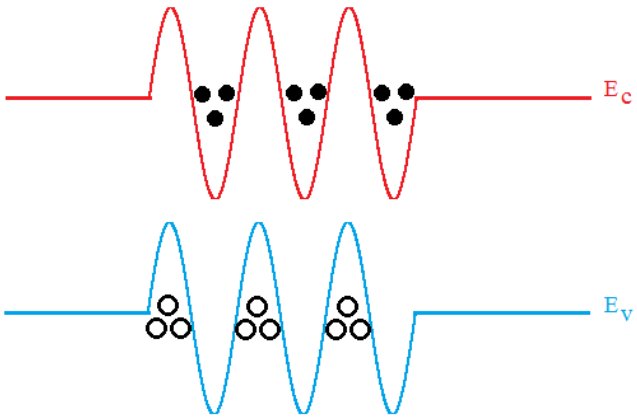

Fig. 1.2.2. Deformation of valence and conduction energy bands caused by a traveling electric potential induced from a SAW. Black solid dots represent electrons being trapped in the wells of the potential. Black circles, open dots, represent holes being trapped.

Attenuation is another aspect of SAWs to consider, most notably when applying them to a 2DEG and/or when a perpendicular magnetic field is applied. Equation 7 shows the attenuation of a SAW [5], where K_{eff} is the electromechanical coupling coefficient, k is the wave vector, σ_s is the conductivity of the material, and $\sigma_M = v_s(\varepsilon_0 + \varepsilon_{GaAs})$ is a constant of the material [6]; which is GaAs in this case.

$$\Gamma = k\frac{K^2_{eff}}{2}\frac{\sigma_s/\sigma_M}{1+(\sigma_s/\sigma_M)^2} \tag{7}$$

$$\frac{\Delta v}{v} = k\frac{K^2_{eff}}{2}\frac{1}{1+(\sigma_s/\sigma_M)^2} \tag{8}$$

Here the attenuation occurs because part of the longitudinal electric field of the propagating wave couples into the electrons of the 2DEG. This not only causes a current to flow but pulls power from the SAW due to ohmic losses. This attenuation is described by Eq. 7. A SAW velocity shift is also observed due to the piezoelectric stiffening of the substrate, see Eq. 8 [5]. Below are the recreated graphs from *ref* 5 to show the relationship of the attenuation and sound velocity shift due to a change in conductivity. As a magnetic field is applied to the material there is a change in the conductivity of the system. In the case of a GaAs/AlGaAs 2DEG the conductivity is very sensitive to these field changes and thus can cause large shifts in attenuation and sound velocity. Most notably from Fig. 1.2.3a as $\sigma_0 = \sigma_M$ the attenuation becomes the greatest which can be seen in the measurement results, see Chapter 4.

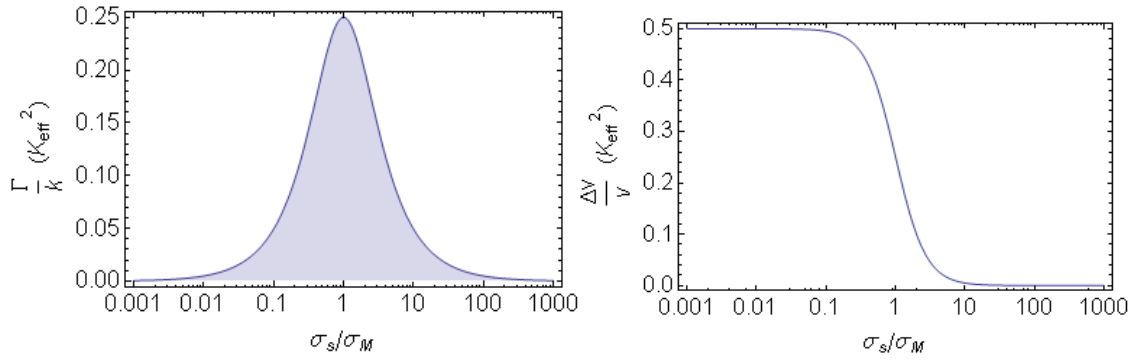

Fig 1.2.3. (a) The SAW attenuation in units of K_{eff}^2, see Eq. 7. (b) The change in SAW velocity in units of K_{eff}^2, see Eq. 8.

1.3 Surface Acoustic Wave Generation

There are several ways in which a SAW can be generated. Some forms can be through lasers, oscillating mechanical stress, and through the use of interdigital transducers (IDTs) [1-2]. The main focus of this work involves SAW generation through IDTs. IDTs are the most commonly used method for SAW generation. Their commercial market capabilities have been used for many years. Their main use is in the area of RFID tags and delay lines for satellite receivers, common to GPS systems. Since the SAW velocity, which is the speed of sound of the material, is much slower than that of the speed of light, *c*, the signal can be properly delayed as to be read by the electronics [1].

The fabrication of IDTs is quite straight forward, although there are many other effects to consider such as proper impedance matching through designing the capacitance and inductance of the IDT to fit the required frequency spectrum [1-2,7]. Another effect

that may need to be considered is the bandwidth itself. Since for my purposes I wanted to attain a single frequency, or small bandwidth, which only needed a small amount of power so the above mentioned effects can be ignored. Though these can be placed aside for experimental purposes it is important to retain those considerations for commercial applications; the details of which are outside of the scope of this research.

The basic structure of an IDT consists of a comb like structure which involves the use of metallic gates patterned on top of a piezoelectric material. IDTs consist of the larger metallic pads in which an rf line is electrically connected, and then there are the IDT fingers (comb structure). The spacing of the fingers, or pitch, determines the wavelength of the SAW [1,7]. To start, use Eq. 7

$$v_s = \lambda f \tag{7}$$

where v_s is the sound velocity of the material, λ is the SAW wavelength which is also equal to the pitch of Fig. 1.3.1a, and f is the frequency of the SAW which is also applied rf frequency. When patterning the IDT it is most common to use a metallization ratio of 0.5 which will produce only odd harmonics [1]. To achieve this ratio the fingers are patterned with a width of $\lambda/4$, and also a finger spacing of equal measure. The number of finger pairs can be used to determine the bandwidth of the IDT and is given by $BW\% = f/N_{pairs}$. Where f is the frequency and N_{pairs} is the number of finger pairs, two adjacent fingers constitute a pair.

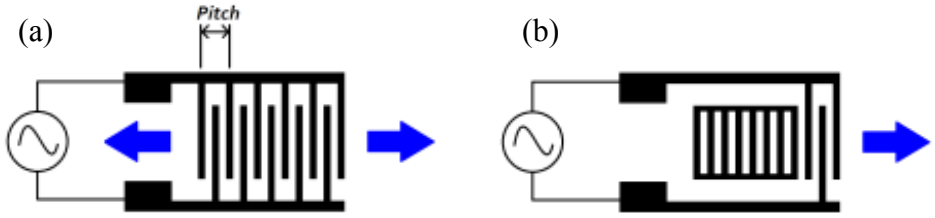

Fig. 1.3.1. (a) Bidirectional IDT which launches SAWs in two directions. The pitch is equal to the SAW wavelength, λ. Arrows show direction of SAW propagation. (b) Unidirectional IDT which uses a Bragg reflector on one end to reflect the wave allowing the full SAW power to move in the direction indicated by the arrow.

Another addition to the IDT design is the use of Bragg reflectors [1,7]; this can be seen in Fig. 1.3.1b. Bragg reflectors are used to turn a bidirectional IDT into a unidirectional IDT focusing the acoustic power into one direction; this is common in commercial applications. From Fig. 1.3.1a the IDT configuration without a Bragg reflector launches SAWs into two directions. With this, half of the SAW power propagates into each direction and it may be desirable to choose one direction since most applications will have their detection electronics on one side of the IDT. The Bragg reflector shown in Fig. 1.3.1b is placed a distance of $\sim n\lambda/2$ away from the IDT fingers; n meaning they are placed an integer number of half wavelengths away. The reflector will have the same geometry as the IDT itself, meaning the same finger spacing and width, and the electrodes will be shorted to one another [1]. There are other forms of reflectors which can be chosen as well but the configuration in Fig. 1.3.1b is typically the most

common. The use of a reflector will reduce or eliminate the reflections from the sample which can cause undesired effects.

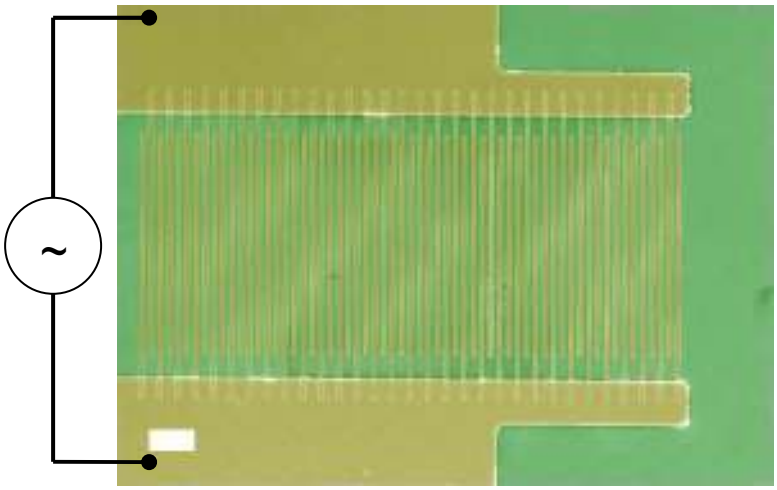

Fig. 1.3.2. Scanning electron micrograph (SEM) image of a fabricated IDT that was used in the work presented. The white scale bar is 10 μm. The gold color indicates the Ti/Au metallic electrodes and the green color indicates the GaAs/AlGaAs heterostructure. The fingers are formed with a metallization ratio of 0.5 with a finger width of 1 μm and equal spacing. The operational frequency is f = 840 MHz, N_{pairs} =30 and has a bandwidth of 28 MHz.

A fabricated bidirectional IDT is shown in Fig. 1.3.2. The schematic to the left of the image indicates where the applied rf signal is connected. The aperture of the IDT is the region where the fingers overlap, in the case of Fig. 1.3.2 it is 50 μm. The operational frequency was found to be 840 MHz. This was done by doing a current vs. frequency sweep, see section 4.3. At non resonant frequencies, the frequencies that reside outside of the bandwidth, no acoustic power is being generated from the IDTs and thus no current

will flow. Once the resonant frequency is applied SAWs will be generated and an acoustic current can then be detected.

1.4 Introduction to Quantum Point Contacts

Quantum point contacts (QPCs) are a useful and widely used tool for probing low dimensional systems and can offer a lot of information and be used in devices such as quantum computing. It has the unique property of being able to quantize current and electronically achieve one dimension systems. The conductance of a QPC is quantized [8-9] and shows steps/plateaus at integer multiples of the $2e^2/h$, where e is the electron charge and h is Planck's constant.

A QPC can be formed in two ways; one is by fabricating a metallic split gate on top of the material, in this case a GaAs/AlGaAs heterostructure with a 2DEG embedded below the surface. Another way is to etch a groove into the 2DEG separating two gates from the center 2DEG region. The two gates in this case will require ohmic contacts so a negative DC bias can be applied. In either case, a negative DC voltage is applied to the gates to constrict the conductance channel into one dimension and eventually pinch off the current. The device presented was fabricated with a top gate structure through metallization.

The electrons, majority carriers, are confined in the z-direction through the inherit properties of the 2DEG and have two degrees of freedom in the x and y directions. As a

potential is being created by the application of a negative voltage on the gates the electrons from the 2DEG see a saddle-point potential [10]. In the z direction there is a quantization of energy levels as the geometry is constricted to the narrow height of the 2DEG. The x direction, which is perpendicular to the current flow, will see a parabolic confinement which is like the harmonic oscillator; $\frac{1}{2} m^* \omega_0^2 x^2$. The energy dispersion is given by

$$E_n(k_y) = \frac{\hbar^2 k_y^2}{2m^*} + E_{n,x} + E_z \tag{8}$$

$$E_{n,x} = (n - \frac{1}{2})\hbar\omega_0 + eV_0 \tag{9}$$

where e is the electron charge, V_0 is the bottom of the confinement potential, $\hbar\omega_0$ is the energy level separation, k_y is the wave vector for the y direction, and n is the subband for the x direction. The energy in the z direction, E_z, is assumed to be the lowest energy subband of the 2DEG since the confinement in that direction is so strong.

Equations 8 and 9 describe the energy in a one dimensional subband because the energy levels are quantized in the x direction and not in the y direction since the electrons are free to move. From Fig. 1.4.1a the one dimensional subband dispersion can be seen versus the wave vector k_y. The electron states in the source and drain leads are filled to their respective chemical potentials μ_s and μ_d. The current is then determined by the

number of subbands that lie below, or in between, the two potentials. Figure 1.4.1b shows the pinch off characteristics of a QPC. As the gate voltage becomes more negative the channel becomes narrower and single electron transmission can be observed. In the graph there is no magnetic field applied thus spin splitting isn't shown. The 0.7 effect is not shown as well.

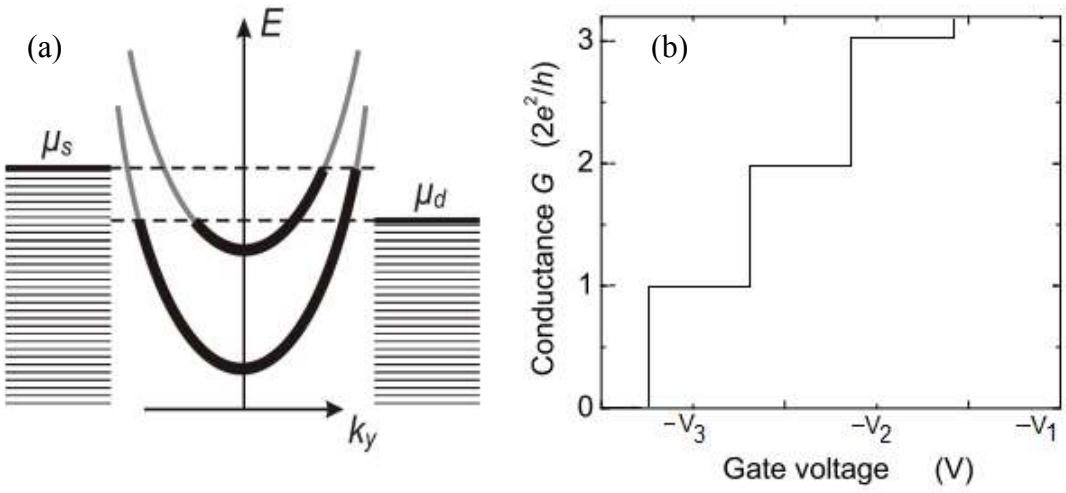

Fig. 1.4.1. (a) One dimensional subband energies as a function of k_y. The source and drain lead energy levels are filled to their chemical potentials μ_s and μ_d. (b) The QPC conductance, G, plot showing quantized steps of $2e^2/h$ as a function of gate voltage; $-V_3 < -V_2 < -V_1$. No magnetic field is applied; hence, no spin splitting is shown.

CHAPTER 2

◄ General Device Fabrication ►

2.1 Material

The work presented uses a GaAs/AlGaAs heterostructure containing a 2DEG 40 nm below the surface and a 400 nm thick sacrificial layer which is wet etched to produce a suspended nano structure, further device details are in later chapters. Figure 2.1.1 shows the details of the layer structure which was grown through molecular beam epitaxy (MBE).

The sacrificial layer is grown as consecutive AlAs/GaAs layers. Though the stoichiometry is different than that of an AlGaAs single layer the effective etching techniques remain the same. The GaAs quantum well has two Silicon delta-doped layers which contribute carriers to the 2DEG once the temperature becomes low enough to activate the 2DEG. These delta doped layers are spaced in such a way to be close enough to the quantum well to contribute carriers but far enough away to avoid impurity scattering.

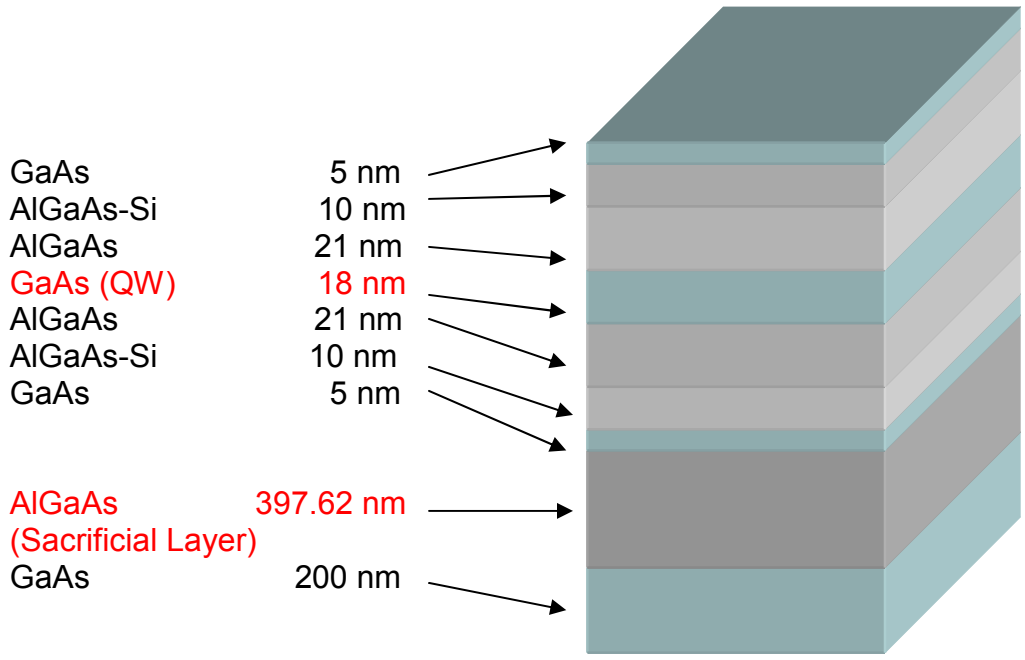

Fig. 2.1.1. Layer sequence of GaAs/AlGaAs 2DEG grown through MBE. The quantum well (2DEG) is around 40 nm below the surface. The sacrificial layer is later removed by wet etching to produce a suspended nano structure.

2.2 Fabrication

Here the details of device fabrication will be discussed. Since the device itself requires multiple steps to achieve the required design a detailed view is necessary to understand the process. The GaAs/AlGaAs heterostructure defined in section 2.1 was used for the device and the steps are shown in Fig. 2.2.1. Figure 2.2.1a shows the 2DEG mesa that is defined in light blue. First the material is spin coated with photoresist (PR) and through optical lithography the mesa structure is defined. After developing the PR

the sample is then placed into a solution of H_2SO_4:H_2O_2:H_20 with a ratio of 3:2:100. The sample was in the solution for 30 sec. to 1 min. The wet etch removes the GaAs/AlGaAs material to a depth of 90 to 100 nm. The etch depth should be below the 2DEG quantum well itself. In Fig 2.2.1b ohmic contacts are added. This is done my coating the sample with PR and through optical lithography defining the four ohmic contact regions. Then through e-beam metal evaporation a sequence of Ni/Au/Ge/Au – 5/10/25/10 nm was deposited. The sample was then annealed in a rapid thermal annealer (RTA) at 450° C for 45 sec. to 1 min.; this would vary depending on metal quality (contamination) and slight differences in one batch of material to another. In Fig. 2.2.1c the sample again was coated with PR and through optical lithography the wire bonding pads and leads of the electrodes for the IDTs and QPCs were defined and metal was added, Ti/Au – 5/100 nm. Titanium (Ti) is used as an adhesion layer.

Figure 2.2.1d shows the addition of the QPCs. The sample was first coated with PMMA and then through the use of e-beam lithography the QPC gates were defined which connect to the optically defined gates from Fig. 2.2.1c. After the QPCs were defined and metal was deposited, Ti/Au – 5/50 nm, another PMMA coating was added and again through e-beam lithography the IDT fingers were patterned, Fig. 2.2.1e, and metal was deposited; Ti/Au – 5/50 nm. The final lithography step is seen in Fig. 2.2.1f were the acoustic waveguide, trench, is defined. The sample again is coated with PMMA and the trench is defined through e-beam lithography. The code used to generate the smooth exponential waveguide geometry can be seen in Appendix A. The code created a

CAD file in DesignCAD 2000 LT which was executed by NPGS to create the waveguide. The waveguide trench width was 300 nm.

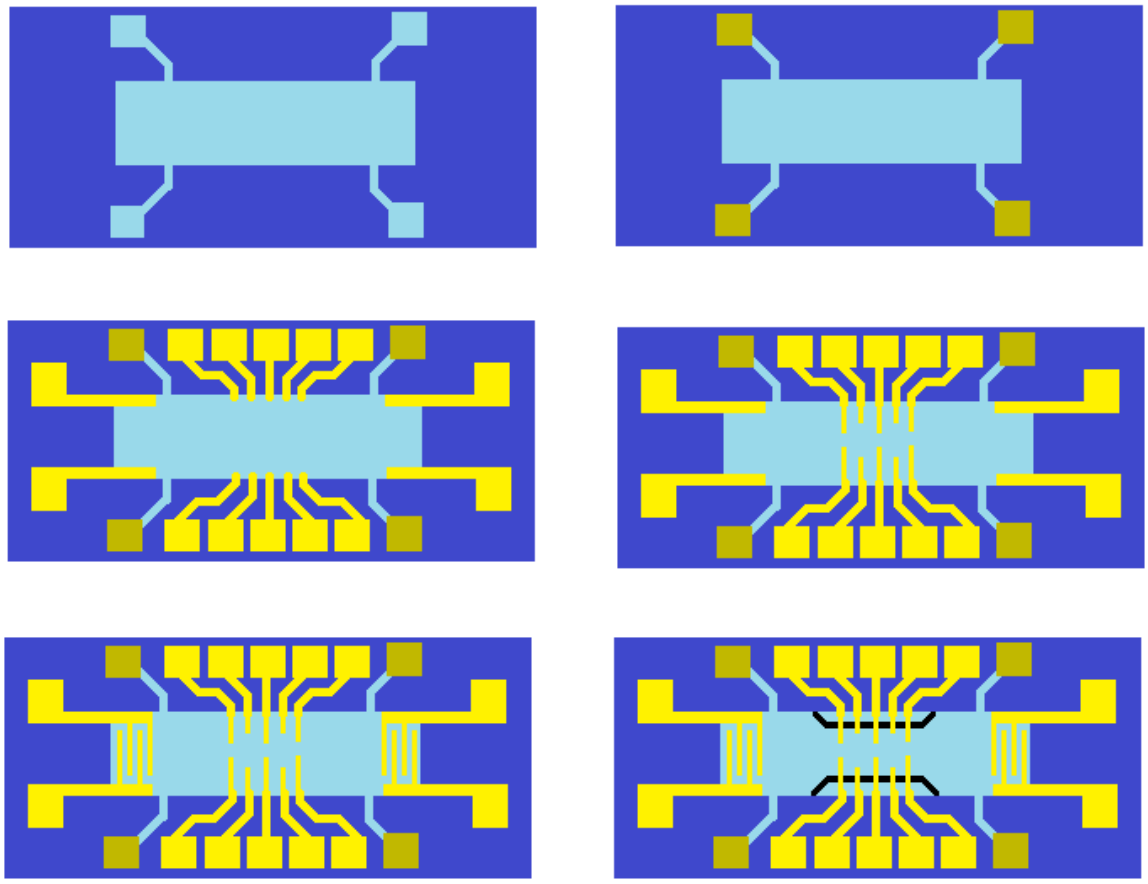

Fig. 2.2.1. Fabrication sequence of device, not drawn to scale. (a) Mesa is defined through wet etching. (b) Ohmic metal is laid down and annealed. (c) Large electrodes are added. (d) QPCs are defined. (e) IDT fingers are defined. (f) Acoustic waveguide is defined and etched. Afterward the sample is wet etched to remove the sacrificial layer and suspend the center region.

The etching of the waveguide, trench, was done using two different methods: deep reactive ion etching (DRIE) and wet etching. Wet etching was done using

H_3PO_4:H_2O_2:H_20 with a concentration of 3:2:100. The Phosphoric Acid solution was chosen over the Sulfuric Acid solution because it has a slower etching rate and showed to be more anisotropic, thus keeping the etch trench width closer to the lithographically defined width. The sample was put into the etching solution for about 3.5 to 4 min. in an ultrasound. The PMMA acted as an etch mask during the process. Once the etch time exceeded 4 min. the PMMA showed signs of degradation. The other approach of etching was done using a DRIE method through the use of an inductively coupled plasma (ICP) system. Various testing was done to unsure the right gases and rf powers of the system to produce a non aggressive etch rate. The real test was to use a PMMA mask as an etch mask. The main etching gas was Chloride (Cl) which has a selectivity of nearly 1:1 between PMMA and GaAs. For this method several layers of PMMA were used to coat the sample prior to the e-beam lithography step, Fig. 2.2.1f. No damage was observed on the surface of the device after DRIE etching, although there was a decrease of about 40% in the electron carrier density as compared to wet etching. This change in carrier density is common for DRIE etched devices containing a 2DEG.

The final step of the process was to then create the suspended center region of the sample where the QPCs lie. This was done through the use of diluted HCl to remove the sacrificial layer, see Fig. 2.1.1. As one batch of wafer material differed by another so the etch times differed as well but most fit within the 30 sec. to 1.5 min. time frame. The time was chosen to suspend the center region of the nano bridge where the QPCs lie and to reduce etching farther regions for the sake of avoiding a long suspended bridge structure

that may collapse. The suspended region usually was about 8 μm in length and through SEM imaging proved to still be suspended. After the sacrificial layer has been removed the sample was then dried. One method of drying was through the use of a critical point dryer, where the sample was immerged into isopropyl alcohol (IPA) and then placed into the dryer. Within this process the IPA is replaced with liquid CO_2 and then heated to remove the liquid CO_2. Liquid CO_2 is used because of its low surface energy causing nearly no capillary forces that would ordinarily collapse the suspended bridge. Another method that was employed, with much success, was to simply immerse the sample in IPA after the sacrificial layer was removed and then take it out of the IPA and use a Nitrogen air gun to blow off the IPA. This saved a lot of time in developing samples.

Figure 2.2.2 an optical image of the device is shown. On the four corners of the device there are the ohmic contacts which are used to measure current through the system, whether it be acoustoelectric current from the SAWs or applied DC current through the adjacent set of ohmic contacts. These four contacts are visible by their "bumpy" appearance which is a result of annealing. The remaining Gold contacts and electrodes are connected to the center QPCs and the IDT fingers.

These larger more visible electrodes are where the device is wire bonded and have the 2DEG around them wet etched away so there is not leakage current. The 2DEG mesa can be easily seen in the center region with four legs, see Fig. 2.2.1a as a comparison. At the very center, shown as silver, is where the QPCs lie, although the details cannot be

seen clearly in Fig. 2.2.2 they are visible in Fig 2.2.3 and Fig. 2.2.4. See Fig. 1.3.2 for IDT details.

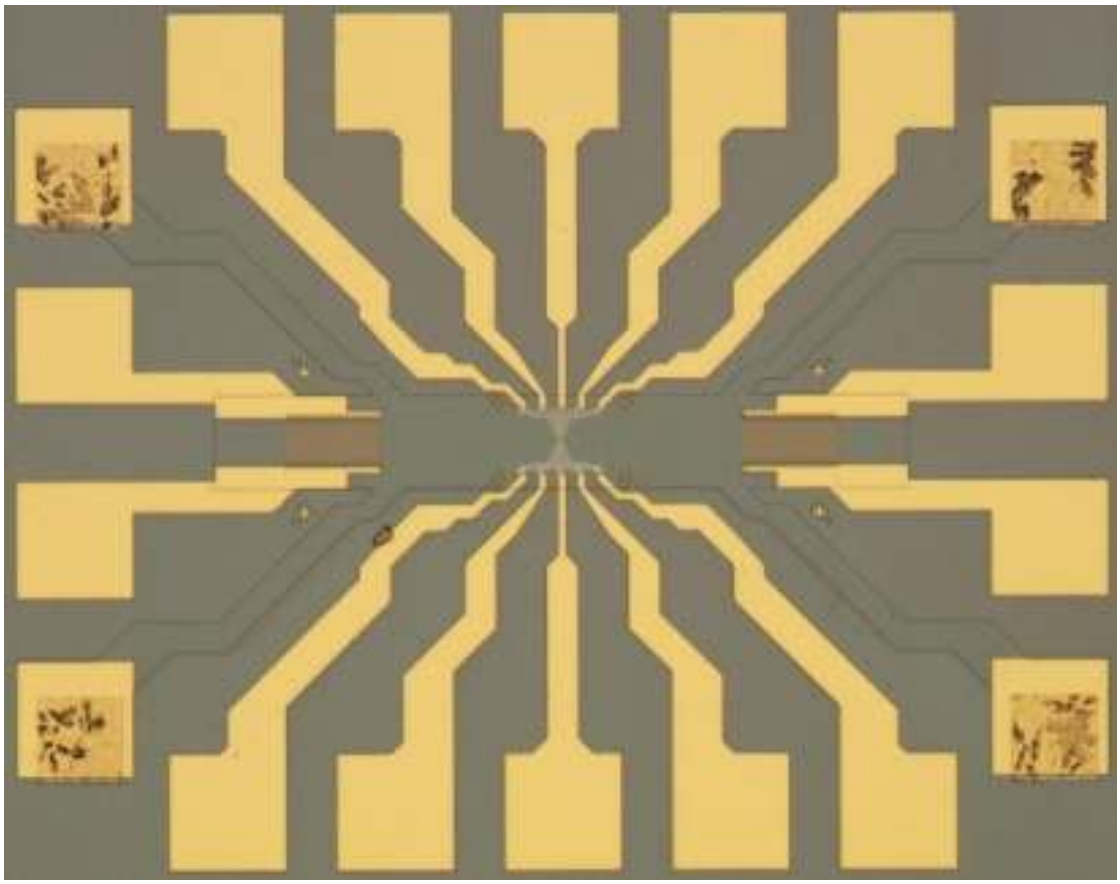

Fig. 2.2.2. Optical image of the device. At the four corners are the ohmic pads which are visible by their "bumpy" annealed metal. The IDT fingers are shown to both the left and right of the center region. The center QPC region, silver color, is where the QPCs lie. The outer mesa defined 2DEG shows that the acoustoelectric current and source-drain current cannot flow outside of the QPC region and be detected by another ohmic contact.

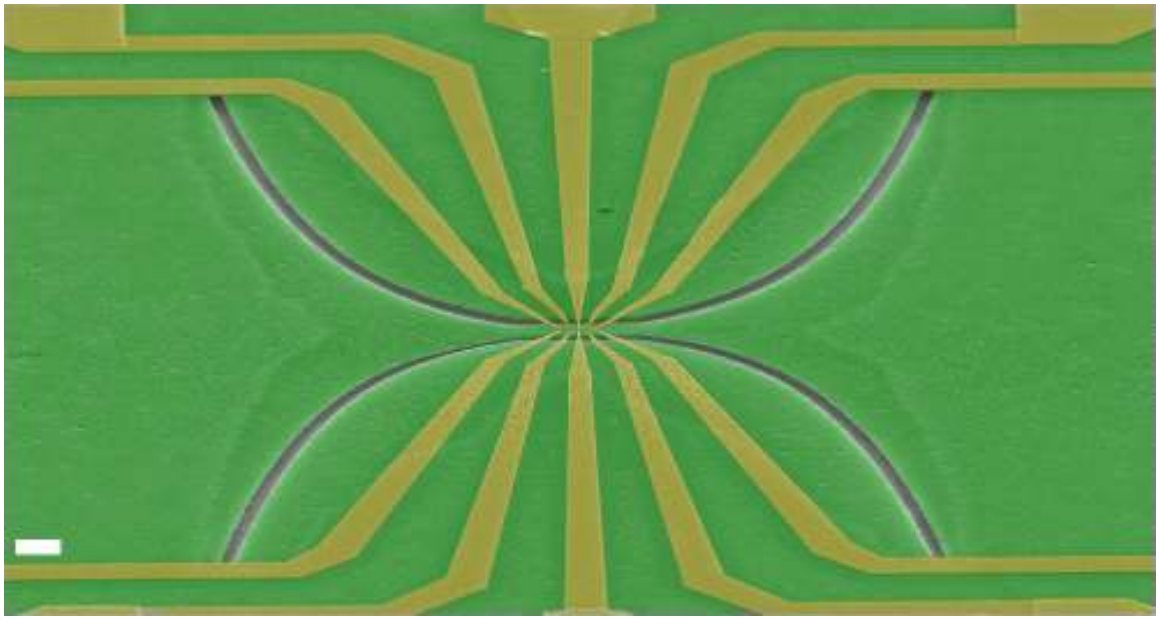

Fig. 2.2.3. Colorized SEM image showing a zoomed picture of the center region of Fig. 2.2.2. Scale bar is 2 μm. The dark trench lines define the acoustic waveguide. Gold color indicates the Ti/Au electrodes and green is the 2DEG region. The darkened green region which outlines the trench lines indicates a suspended structure.

In Fig. 2.2.3 the center region of Fig. 2.2.2 becomes easier to distinguish. The gold color indicates the Ti/Au electrodes which make up the center QPCs and the green color is the 2DEG. The acoustic waveguide is now visible which appears as the dark trench curve; see section 2.3 for details on the acoustic waveguide. Around the acoustic waveguide trench the region appears as a darker color, dark green in this case. This darker color appears because of a height difference in the material. Dark colors are lower in height than the lighter colors.

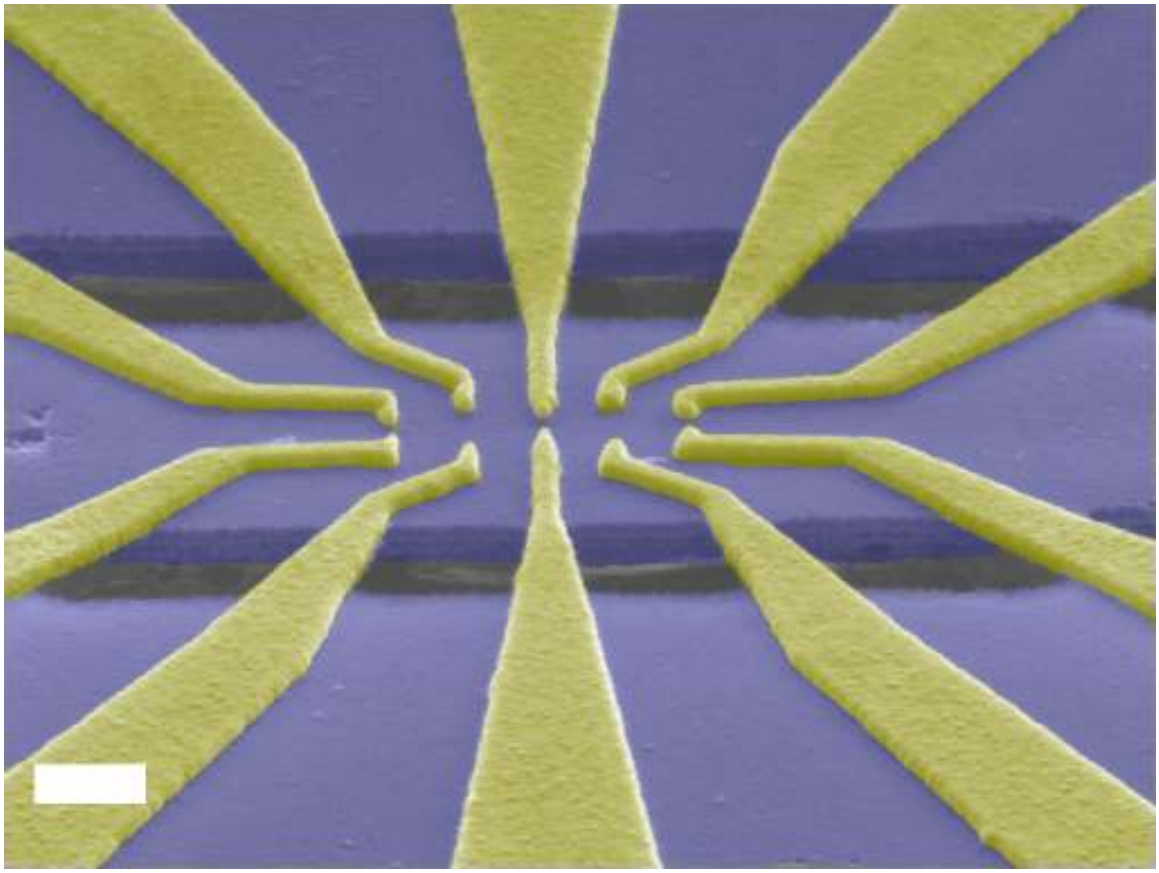

Fig. 2.2.4. Colorized SEM image of the center region of Fig. 2.2.3. Scale bar is 300 nm. Gold indicates the Ti/Au electrodes and blue is the 2DEG region. The width of the tip of a QPC finger is ~80 nm. The edges indicate the trench line for the acoustic waveguide. Slight bending of the center beam indicates a suspended structure.

This color difference is because the SEM operation. Objects that are higher in height are closer to the detector and thus electrons do not have to travel as far and also the electron flux to the detector is slightly higher causing a brighter image. The darker regions are farther away from the detector, slightly decreasing the electron flux. Also, the suspended region is a thin membrane, 90 nm, and electrons may penetrate through the

membrane and be unable to cause addition secondary electron scattering which the detector can pick up causing a lower electron flux and darker image. It is a general rule that a dark region in SEM images indicates a suspended region.

In Fig. 2.2.4 the center region of Fig. 2.2.3 can be easily distinguished. Here, the fine structure of the QPCs, gold color, is visible. The e-beam defined electrodes taper down to an 80 nm tip. There are five pairs of QPCs each being about 225 nm from one another and an opening of 80 nm for the left, center, and right pair and an opening of 120 nm in the 2^{nd} and 4^{th} pairs. The electronic characteristics are measured and shown in later sections. The device itself is set up in such a way that acoustoelectric current can only flow through the region defined in Fig. 2.2.4 with the aid of the acoustic waveguide; as well as, the DC current is restricted to this region since the electrodes electronically block current elsewhere in the device.

2.3 Acoustic Waveguide

From section 2.2 we've seen the device layout and the fabrication steps were well detailed along with images of the real device. Here the design and operation of the acoustic waveguide will be discussed. The acoustic waveguide can be seen in Fig. 2.2.3 as the dark etched trench which is straight in the center region and exponentially curves outward as it moves farther away from the center region.

Acoustic waveguides can be fabricated in several different geometries; conical, pipe, parabolic, and exponential. Each of these geometries has its own uses and advantages. Here, for this device, the exponential and pipe geometries are used. The pipe geometry is best suited for the center straight region of the waveguide where the QPCs themselves reside. The exponential geometry is used to guide the SAWs down into the pipe region of the waveguide. The exponential waveguide was chosen over the conical waveguide because it can be locally fabricated with a minimal size of geometry. A conical waveguide, to be effective, must be fabricated from the center region where the QPCs reside all the way to the IDTs themselves. This is a disadvantage because the conical geometry does not open up wide enough to cover the IDT aperture and would not allow all of the acoustic power to enter into the center pipe region. Also, e-beam lithography has a limited window size in which it can write. To write across such a large distance of >232 μm with a small etch window would require the movement of the SEM stage and thus alignment would be lost resulting in an undesirable feature.

To start to understand the use and function of the acoustic waveguide we need to go over some of the background. We first start off with Webster's Horn Equation

$$\frac{d^2\phi}{dx} + \frac{d(ln(S))}{dx}\frac{d\phi}{dx} - k^2\phi = 0 \tag{10}$$

where k is the wave vector, S is the cross sectional area of the horn (waveguide) as a function of x, and ϕ is the velocity potential. Here we can set up the equation as a sum of two waves representing the outgoing wave (diverging) and reflected wave (converging) as, $\phi = Au+Bv$; where A and B represent the diverging and converging waves, respectively. The solutions to Eq. 10 are given in terms of absolute acoustical impedance. For a pipe geometry, which the center region of the device, the B term is zero since there are no reflected waves. Equation 11 then gives the impedance of the pipe geometry

$$z_A = \frac{\rho_0^{v_s}}{S_t} \tag{11}$$

where ρ_0 is the density of the material (GaAs), v_s is the sound velocity in the material, and S_t is the throat area of the pipe geometry. From Eq. 11 the impedance of the pipe waveguide is a constant. In order to guide the SAWs into this smaller region we need to add an additional section of waveguide to the system, in this case exponential waveguide geometry. Again, the exponential waveguide was chosen because it opens up very quickly and has small footprint. The impedance of an exponential waveguide is given by Eq. 12 [11]

$$z_A = \frac{\rho_0^{v_s}}{S_t}\left(\sqrt{1-\left(\frac{f_c}{f}\right)^2} + iT\frac{f_c}{f}\right)\left(1-\frac{f_c^2\left(1-T^2\right)}{f^2}\right)^{-1} \tag{12}$$

$$z_A = \frac{\rho_0^{v_s}}{S_t}\left(\sqrt{1-\left(\frac{f_c}{f}\right)^2}+i\frac{f_c}{f}\right) \tag{13}$$

where f_c is the cutoff frequency of the waveguide, and T is a parameter describing the curvature of the waveguide; in the case of an exponential waveguide T = 1. An exponential waveguide acts as a high pass filter. In the design of the device used the cutoff frequency, f_c, was chosen to be 75 MHz. The operating frequencies of the device are ≥840 MHz which are well above cutoff and cause the impedance of the exponential waveguide to match that of the pipe waveguide. Also, the impedance given in Eq. 12 is a general impedance for a series of horns, or acoustic waveguides. Since for our parameter T is unity, Eq. 12 reduces to Eq. 13. When looking at Eq. 13 and comparing the ratio of f_c/f we get 0.089 for 840 MHz and 0.05 for 1.488 GHz; the two operational frequencies of the devices used.

Now let's take a look at the geometry itself. This is governed by the equation derived by Salmon [11]

$$S = S_t\left(Cosh\frac{x}{x_0}+T\times Sinh\frac{x}{x_0}\right)^2 \tag{14}$$

$$x_0 = \frac{v_s}{2\pi f_c} \tag{15}$$

where S is the is the wave front area expansion, or also, the area of the waveguide geometry. It can be seen in x_0 that the cutoff frequency term resides in the denominator. As mentioned before the cutoff frequency was chosen to be 75 MHz because the curvature of the waveguide fits nicely to the device in that it allows a large opening, 80 μm, and has a small footprint which can sit inside of the e-beam lithography drawing window, thus eliminating any addition stage movements and realignments. The geometry of the waveguide also fits around the electrodes, see Fig. 2.2.3, allowing minimal to no interference on the electrodes from the electric field produced by the SAWs as they enter the waveguide.

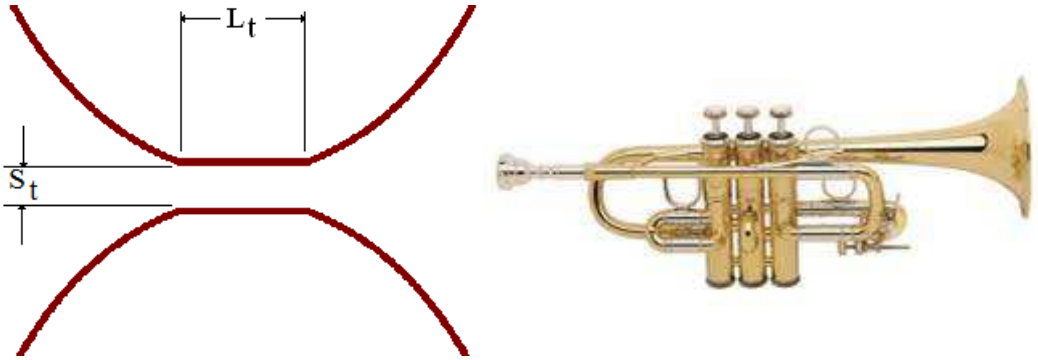

Fig. 2.3.1. (a) General layout of curvature for an exponential waveguide with throat width (opening) of S_t, which is also the pipe waveguide opening. L_t is the length of the pipe waveguide. (b) Trumpet showing a hyperbolic form of an acoustic waveguide.

Figure 2.3.1a shows a general curve that illustrates the geometry used in the device. The parameter S_t from Eqs. 12-14 can now be seen as it relates to the device

geometry. This parameter was chosen to be 2 μm to allow a narrow enough bridge to remain and also hold up against the wet etching process which will increase the etch trench width. From Fig. 2.3.1b a standard example of an acoustic waveguide is shown which most people will be familiar with. The opening of the trumpet which leads to the open air is a waveguide that fits in the hyperbolic family of acoustic waveguides, just like our exponential waveguide.

In conclusion, the details of device fabrication along with the design parameters have been explained. The device has two IDTs, five QPC pairs, four ohmic contacts, an acoustic waveguide trench, and the center region is suspended. This setup allows several different phenomena to be tested. In the next sections the testing setup and results will be displayed using the device detailed in this section.

CHAPTER 3

◄ Measurement Setup and Design ►

3.1 Insert

The system used to measure the device consisted of 3rd party parts as well as in house built parts. The cryogenic measuring system consists of a dewar which has an inner vessel which holds liquid Helium (Lhe) and an outer vessel which contains liquid Nitrogen (LN). Within the dewar is an Oxford Instruments insert which consists of a 9 T superconducting magnet with a Lambda point refrigerator. The sample insert, which was made in house, is inserted into the dewar and fastens to the Oxford Instruments insert while the sample section of the insert sits in the center of the magnet.

Figure 3.1.1 shows the insert that was created for testing purposes. The upper half of the device is made from Stainless Steel and the lower section is made from Oxygen free high conductivity (OFHC) Copper. Stainless Steel is used on the top section because of its low thermal conductivity. This is needed since the portion of the insert that connects, or is fastened, to the dewar will always be at room temperature. Atop the insert

are several DC wire connectors and four rf line connectors. The DC wiring connected from the top down to the first powder filter stage is made from Phosphor-Bronze wire in a twisted pair fashion. This wire metallurgy was chosen because of its low thermal conductivity which prevents heat from the top side room temperature bath. The thermal conductivity is 48 (W/m K) as compared to Copper which is 400 (W/m K). This is wrapped into an inductor coil with 1 m long wire inside of each powder filter. This creates an AC block, as well as, strong AC signal attenuation through the skin effect of the small powder particles.

The DC lines coming from the Stainless Steel powder filter going down to the sample are Silver coated Copper wires. This allows heat to be quickly transferred away from the sample through its leads while under test. The rf lines of the system are Stainless Steel lines which again have a low thermal conductivity as to disallow heat transfer into the sample. Two rf lines are interrupted by a Sapphire coplanar waveguide. This added feature allows the rf lines to be cooled since Sapphire has a large thermal conductivity at low temperature. The Sapphire coplanar waveguide is housed in an OFHC case, see Fig. 3.1.1.

The system is also equipped with a laser diode which is mounted in such a way that it is perpendicular to the sample surface. This diode emits in the 650 nm wavelength range and is capable of operating at low temperature without carriers freezing out. This is used to illuminate the sample once the 4.2 K temperature is reached to excite more carriers (electrons) into the 2DEG conducting region.

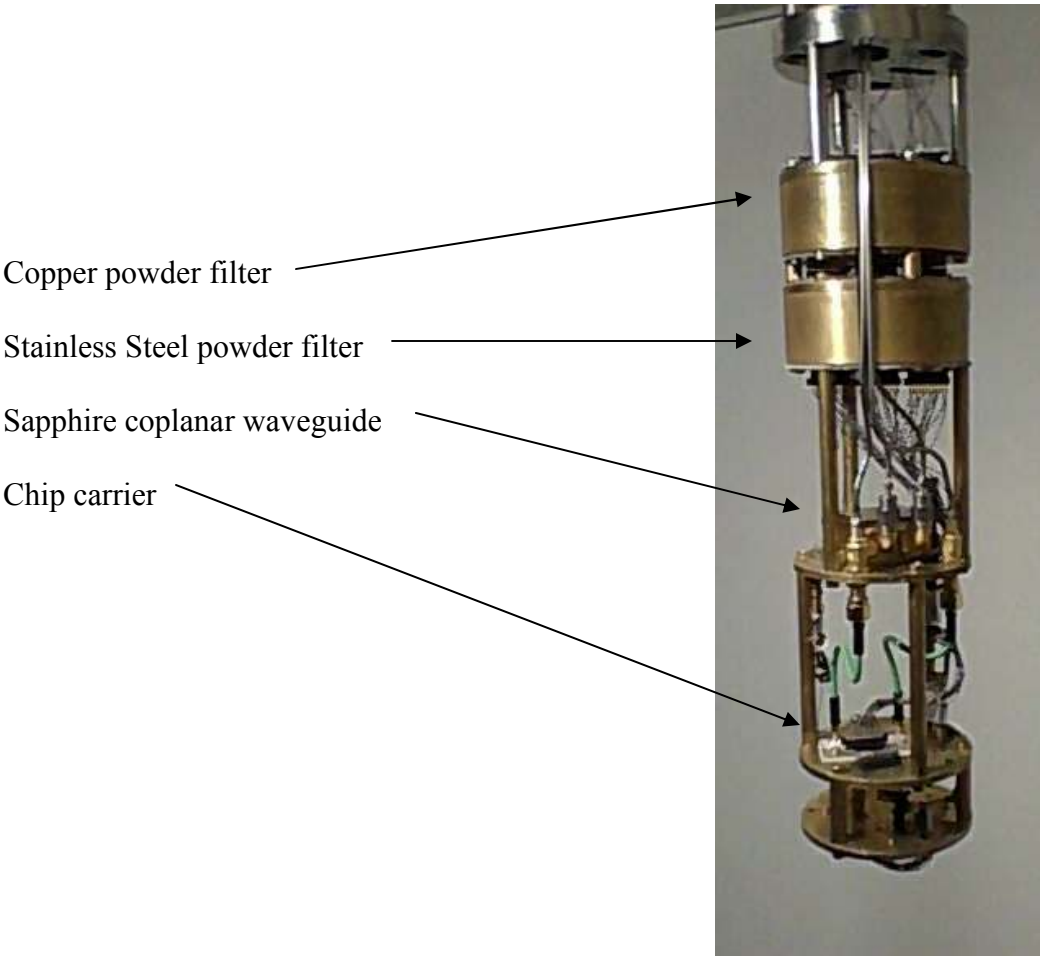

Fig. 3.1.1. Bottom half of insert used to carry out measurements. The major components are listed on the diagram as the Copper and Stainless Steel powder filters, Sapphire coplanar waveguide, and the chip carrier. The system is also outfitted with a lower temperature laser diode.

The insert shown in Fig. 3.1.1 is inserted to a Stainless Steel tube that is first evacuated to about 10^{-6} Torr. Once this vacuum level is reached a small amount of Helium gas is introduced into the system which acts as a coupling gas. The outer vacuum

tube is directly in the LHe bath and the Helium coupling gas transfers heat from the OFHC stage of the system to the LHe bath. Thus, this insert can maintain a constant 4.2 K base temperature.

3.2 Electronic Setup

The measurement setup consisted of the following electronic devices:

Equipment	**Usage**
Princeton Applied Research: 124 A	Lock-In Amplifier
Yokogawa: 7651	Precision Voltage Source
Ithaco: 1211	Current Preamplifier
Agilent: E8257D	RF Signal Generator

Table 3.2.1. Equipment list and usage.

When looking at Fig. 4.3.1 the above equipment from table 3.2.1 is used as follows: The DC source connected to the QPC gates is the Yokogawa, the current amplifier connected to the two ohmics is the Ithaco, the rf signal connected to the IDT is the Agilent signal generator. The Lock-In Amplifier was used for Hall measurements, it was connected to the four ohmic contacts; no schematic is shown.

CHAPTER 4

◄ Measurement Data and Analysis ►

4.1 DC Characteristics of QPC

To characterize the device we need to first know how each component of the device will wok in order to establish operability and basic behavior. Since the goal is to use SAWs to generate current through the nano bridge we need to first see how the QPCs themselves will operate. To establish this we start off by taking the DC measurements of the QPCs on the device. This is done by applying a constant voltage to two of the ohmic contacts and then sweeping the voltage on each QPC pair to get the transport data. For this device the focus will be on the center QPC pair since the symmetry allows for some interesting effects when later applying SAWs as a current source.

All measurements are run with a base temperature of 4.2 K. Because of this higher temperature the quantized steps are washed out due to the thermal background. An ideal case would look something like Fig. 1.4.1b. In Fig. 4.1.1 some of the features are still present but easily lost in the current reading once the QPC reaches near pinch off. Although this result would have been better if run at a lower temperature there is no need in this case. The reason for this is because of the ultra sensitive nature of SAWs with the

2DEG [5]. Later we will see that this behavior of SAWs allows us to still probe into the quantum nature of the device and will reveal the lost features.

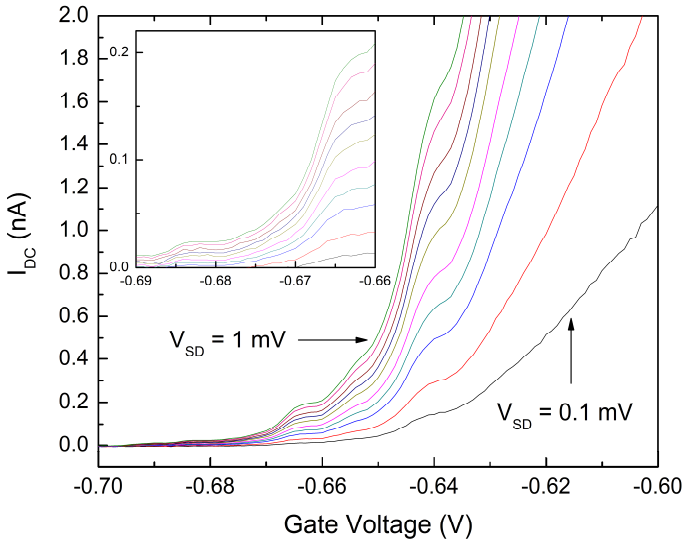

Fig. 4.1.1. Applied DC source-drain bias pinch off with V_{SD} ranging from 0.1 mV to 1 mV in 0.1 mV increments. Inset shows a magnified view of the current with the gate voltage ranging from -0.69 V to -0.66 V. Quantized step features are washed out due to the thermal background.

From Fig. 4.1.1 we see that the device pinches off at -0.7 VDC and there is no more current present, or detectable. The voltage sweep does start from 0 VDC but only a portion is shown for the sake of brevity. The inset in Fig. 4.1.1 shows a magnified view of the -0.69 VDC to -0.66 VDC range; again, some steps are visible but the truly quantized steps are lost. Later when we add SAWs additional features will begin to emerge.

4.2 Hall Measurement and 2DEG Data

To further expand upon the device we need to know about the material, this information will become important in the next sections. Here a standard Hall measurement was performed. This was done with a four-point lock in technique.

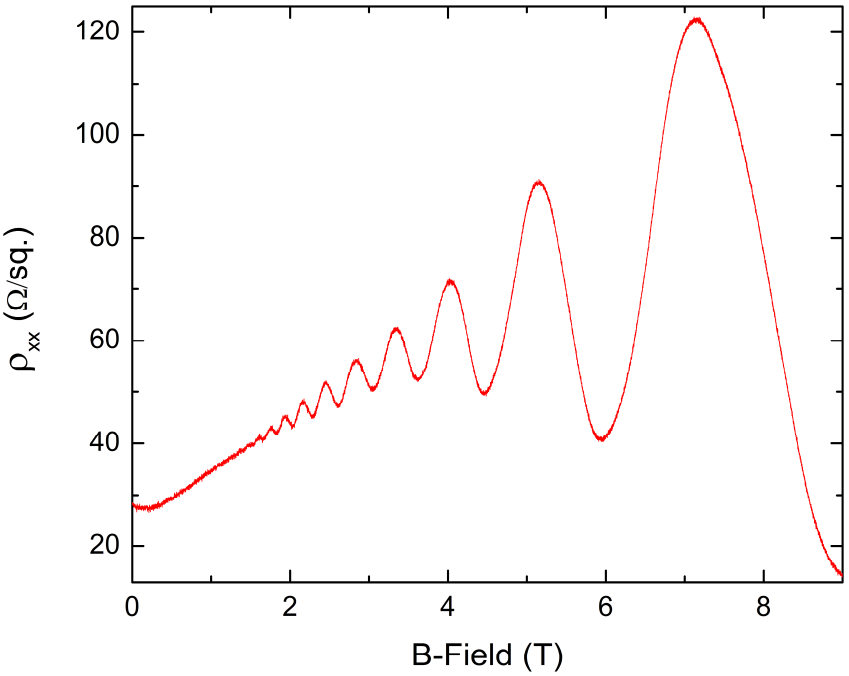

Fig. 4.2.1. Hall measurement data from the device. Measurement was done using a standard four-point lock in technique.

From Fig. 4.2.1 we see the results of the Hall measurement along with the Shubnikov de Haas (SdH) oscillations while sweeping the magnetic field. From these oscillations we

are able to calculate the electron carrier density of the 2DEG along with the electron mobility.

To start getting the material properties we first need to take a look at the background of Hall calculations. We first look at the classical Hall Effect, the main setup for this is shown in Fig. 4.2.2. A constant current source is applied in the x-direction while the induced voltage in measured in the y-direction. This is done with an applied magnetic field in the z-direction.

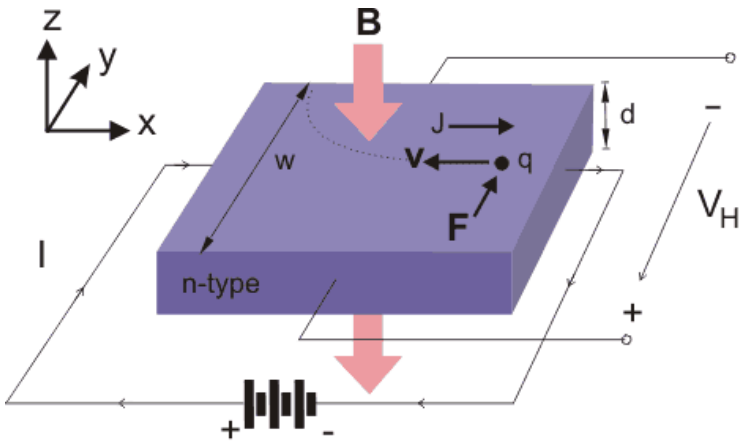

Fig. 4.2.2. Schematic for Hall measurement on a 2DEG. A constant current is applied along the x-axis while the induced voltage is measured along the y-axis.

The Hall voltage, V_H, which is built up in the y-direction is compensated by the Lorentz force which is also in the y-direction [12]. The Lorentz force acting on an electron with velocity v_x in the x-direction is

$$F_y = -e(v \times \boldsymbol{B})_y - eE_y \tag{16}$$

$$F_y = ev_xB - eE_y = 0 \tag{17}$$

where $E_y = V_H/w$ is the Hall field, e is the charge of an electron, and B is the applied magnetic field. Since there is no current in the y-direction the force must be zero which allows us to reduce Eq. 16 to Eq. 17 [12]. For the device in this thesis we have electrons as majority carriers so the calculations will be carried out as such. For this case we have the current in the x-direction as

$$j_x = I/(wd) = -nev_x \tag{18}$$

from Eqs. 17-18 it follows that

$$E_y = \frac{V_H}{w} = -\frac{j_xB}{ne} = -\frac{IB}{newd} \tag{19}$$

It is common to use the Hall constant, $R_H = -(ne)^{-1}$, which can be determined from the measurements given the relation

$$V_H = R_HIB/d \tag{20}$$

The type of carrier can be determined from the sign of R_H, where a negative sign corresponds to electrons and a positive sign corresponds to holes [12]. The carrier concentration is calculated from the absolute value of R_H.

Finally, if the material has both electrons and holes as carriers then the Hall constant is given by [12]

$$R_H = \frac{p\mu_p^2 - n\mu_n^2}{e(p\mu_p + n\mu_n)^2} \tag{21}$$

where n and p are the respective electron and hole carrier densities, μ_n and μ_p are the respective electron and hole mobilities.

To further understand the results, Fig. 4.2.1, from the device to get the desired material parameters we now need to look into the Quantum Hall Effect and the resulting SdH oscillations. Following from section 1.4 we need to continue the treatment of 2DEGs. Again, the electrons are confined in the z-direction and are free in the x- and y-direction. The energy of the electrons is given by [8-9,12]

$$E_j(\vec{k}) = \frac{\hbar^2 k_x^2}{2m_x^*} + \frac{\hbar^2 k_y^2}{2m_y^*} + E_z^j \qquad j = 1,2,3,... \tag{22}$$

where m_x* and m_y* are the effective masses of the electrons for free motion in the x- y-plane. The energy values for the x- and y-directions are that of a free electron and the energy values of the z-direction are the discrete eigenvalues due to quantization and are denoted by E_z^j. The z-direction of the 2DEG is considered a rectangular quantum well of thickness d_z with infinitely high barriers; thus, E_z^j are solutions to the standing electron wave in a box

$$E_z^j \cong \frac{\hbar^2 \pi^2 j^2}{2m_z^* d_z^2} \qquad j = 1,2,3,..... \tag{23}$$

This describes the parabola subbands along the x- and y-directions, see section 1.4. The dimensionality of the 2DEG can further be decreased by applying a perpendicular magnetic field, B, as shown in Fig. 4.2.2. A strong magnetic field forces the electrons into a cyclotron orbit perpendicular to the field with a frequency of $\omega_c = -eB/m^*$ which is determined by the balance of the Lorentz force and the centrifugal force [12]. The orbital movement can be separated into two linear harmonic oscillations perpendicular to one another. The energy eigenvalues of the orbits are harmonic oscillators with eigenfrequency ω_c. The increased quantization caused by the magnetic field effects the subbands and the energy is now written as

$$E_{j,n,s} = E_z^j + (n + ½)\hbar\omega_c + sg\mu_B B \tag{24}$$

where $s = \pm 1$ is the spin quantum number, μ_B is the Bohr magneton, and g is the Lande factor of the electron. The application of a magnetic field and influence on the quantization of energy levels is called Landau levels, which leads to the splitting of energy parabolas into discrete energy eigenvalues [12], see Fig. 4.2.3b.

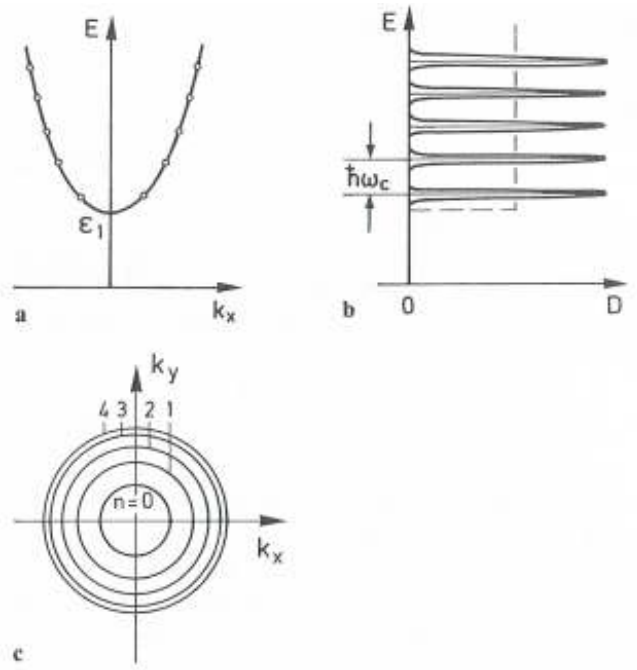

Fig. 4.2.3. Quantization of 2DEG in an external magnetic field. (a) Energy parabola of first subband in the 2DEG along k_x. Points (open circles) are further quantization in the form of Landau levels. (b) Density of states in the first subband, dashed line is without a magnetic field and the peaks are with a magnetic field. The cyclotron frequency, ω_c, of electron orbits in a magnetic field. (c) Reciprocal space representation of Landau splitting.

In the presence of a magnetic field the continuous density of states splits into a series of δ-like peaks that are separated from one another by energies of $\hbar\omega_c$. The number of states is conserved and the Landau levels must contain the same number of states as the case of no magnetic field. This causes a degeneracy of the Landau level which becomes

$$N_L = \hbar\omega_c D_0 \tag{25}$$

where D_0 is the subband state density in the case of $B = 0$. The density of states is a factor of two smaller from the spin degeneracy being lifted by the magnetic field and becomes $D_0 = m^*/2\pi\hbar^2$ and the degeneracy of the Landau level is $N_L = eB/h$. As the magnetic field strength increases the density of states peaks cross the Fermi energy and electrons then occupy the Landau level. This transition is seen as SdH oscillations. All of this is part of the Quantum Hall Effect. The Hall resistance at magnetic fields where the Landau levels cross the Fermi energy are derived from the classical Hall effect which leads to [12]

$$r_H = \frac{V_H}{I} = \frac{-B}{nde} = \frac{-B}{eN_{2D}} \tag{26}$$

Another commonly used form which is used to determine the carrier concentration is

$$n = \frac{2e}{h}\frac{1}{1/B_1 - 1/B_2} \tag{27}$$

where h is Planks constant, and B_1 and B_2 are two consecutive valleys in the Hall measurement data, see Fig. 4.2.1. The other quantity to obtain from a 2DEG is the carrier mobility, this can be calculated using [12]

$$\mu_H = r_H \mu = \frac{V_H}{IR_S B} \tag{28}$$

where R_S is the sheet resistance and I is the supplied current. Given Eqs. 27-28 and the information from Fig. 4.2.1 the 2DEG used for this device has a carrier density of n_e = 4.2×10^{15} m^{-2} and an electron mobility of $\mu_e = 2.57 \times 10^5$ cm^2/Vs.

4.3 Acoustoelectric Current Frequency Response

Another factor to determine is the center frequency of the IDTs. This is done by sweeping the applied rf signal to the IDTs and measuring the acoustoelectric current as it is generated. This can be measured in several ways. The most forward method is to connect an rf signal to the IDTs and let the rf generator run in continuous mode while sweeping the frequency [2,7], see Fig. 4.3.1. At the same time connect a current amplifier to two of the ohmic contacts. If there is a lot of rf noise measured from the

acoustoelectric current in the system other methods can be used. One such method is to amplitude modulate the rf signal to the IDTs and then use a lock-in amplifier to measure the acoustoelectric current with the lock-in frequency being equal to the modulation frequency of the rf source. For the device presented in this thesis the result was the same regardless of measurement technique.

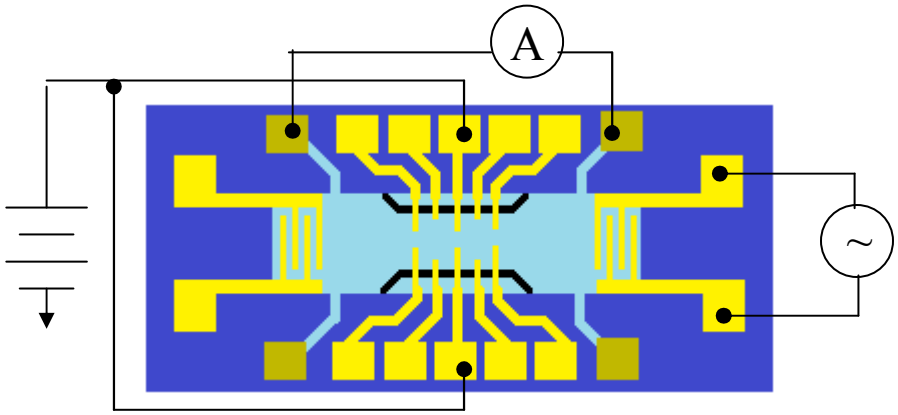

Fig. 4.3.1. Schematic of setup to measure the acoustoelectric current during an rf frequency sweep to determine the center frequency of the IDTs. The gate voltage can be set to floating or ground for a simple scan.

The scan is needed to find the center frequency for two reasons: 1) lithographic errors will cause a frequency shift due to the designed IDT finger width not matching the fabricated finger width, and 2) the layer sequence of the heterostructure will effect the sound velocity, v_s, of the material. The scan presented in Fig. 4.3.2 is used to determine the center frequency of our device. Here the setup shown in Fig. 4.3.1 is used while

applying a pinch off voltage to the center QPC gates. The pinch off voltage is held at -0.8 VDC. This is beyond the DC pinch off region presented in Fig. 4.1.1.

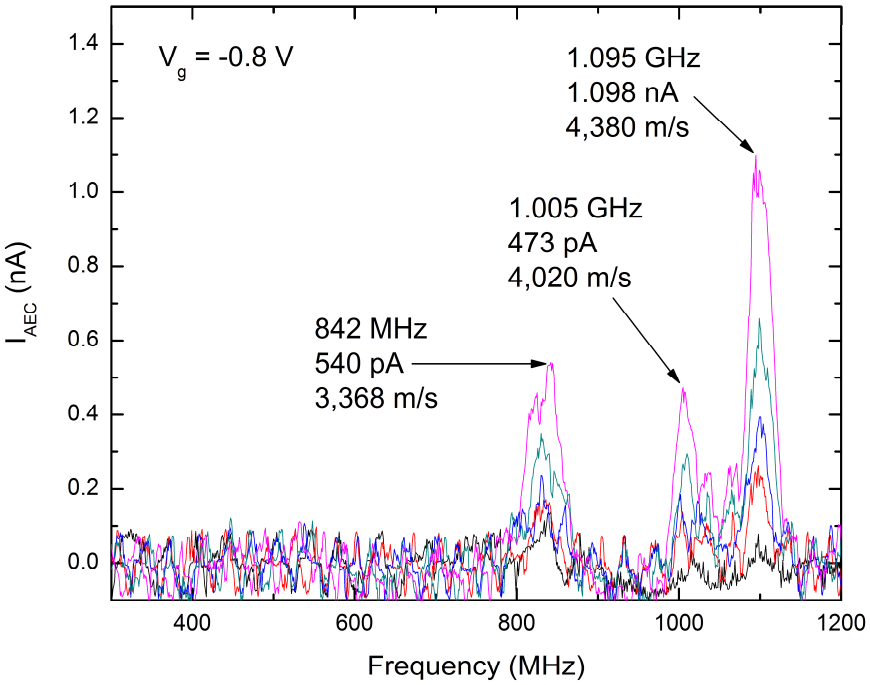

Fig. 4.3.2. Acoustoelectric current vs frequency at different rf powers ranging from -18 dBm to -10 dBm in 2 dBm steps. Center QPC pair is held at -0.8 VDC which is beyond the DC pinch off regime. Different sound velocities correspond to different SAW modes.

The information shown in Fig. 4.3.2 shows several things: 1) Even though the gate bias pinches off the DC current the acoustoelectric current can still penetrate the potential barrier, and 2) different frequencies appear which represent the different modes of acoustic waves [13]. The 842 MHz frequency has a sound velocity of v_s = 3,386 m/s which corresponds to a fast transverse wave [13]. The transverse wave is the one we are

interested in and fits the parameters of Eq. 7 given the results of Fig. 4.3.2. The frequency of 1.095 GHz corresponds to a longitudinal mode [13], and the remaining is a bulk mode. The reason these frequencies appear is because different modes propagate at different sound velocities. This is also effected by the lithographic offset to the (110) direction, which in our case is 10°.

4.4 Acoustoelectric Hall Measurement

As seen in section 4.2 a Hall measurement was performed using a DC bias on the device through two ohmic connections. The standard SdH oscillations were visible as was expected. Here, the same measurement was performed by the use of SAWs generated through the IDTs. The frequency of operation for this device was 1.488 GHz which is the fast transverse mode. The acoustoelectric current trace shown in Fig. 4.4.1a shows all of the features as the standard source-drain bias. The low range magnetic field data shows a large peak; this may be due to the sudden change in the conductivity of the 2DEG. It is most commonly practiced to not include this data in since there are several theories for low field behavior but most devices published on do not exhibit a predictable behavior [5]. From Fig. 4.4.1a the SdH oscillations of the acoustoelectric trace are mismatched from the source-drain bias trace due to a velocity shift of the SAW [5], see Eq. 8. From Eq. 8, as well as Eq. 7, SAWs are very sensitive to changes in the conductivity of the 2DEG.

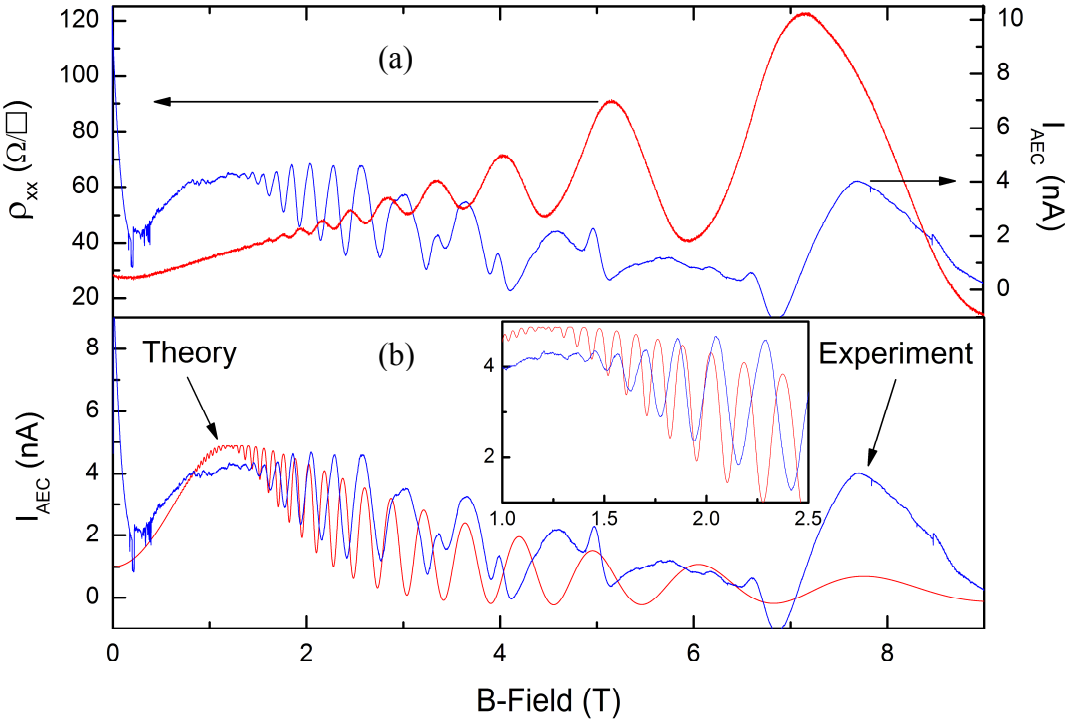

Fig. 4.4.1 (a) Hall measurement data for both a source-drain bias (red trace) and SAW induced current (blue trace). The SdH oscillations are visible in the acoustoelectric trace and the shift in peaks along the x-axis are due to velocity shifts of the SAW. (b) Theory, Eq. 30, (red trace) with experiment (blue trace).

The next step is to now develop a theory which can be used to describe and reproduce the results shown in Fig. 4.4.1a. The first thing needed is a solid theory for the conductivity of a 2DEG in magnetic fields. This is given by T. Ando *et al.* as [14]

$$\sigma(B)=\frac{\sigma_0}{1+\omega_c^2\tau^2}\left(1-\frac{2\omega_c^2\tau^2}{1+\omega_c^2\tau^2}\frac{2\pi^2 k_B T}{\hbar\omega_c}csc\,h\left\{\frac{2\pi^2 k_B T_e}{\hbar\omega_c}\right\}\right.$$
$$\left.\times cos\left\{\frac{2\pi^2 E_F}{\hbar\omega_c}\right\}exp\left\{-\frac{\pi}{\omega_c\tau}\right\}\right) \tag{29}$$

where k_B is the Boltzmann constant, T is the temperature of the bath which is 4.2 K, T_e is the electron temperature. Here the electron temperature is the same as the bath temperature since we are operating at a high temperature of 4.2 K. Equation 29 is used to describe the conductivity parameter in Eq. 7. In Eq. 7 σ_S is replaced with Eq. 29 and the value is normalized, given the following

$$\frac{J(B)}{J(0)} = \frac{\sigma(B)/\left(1+\left(\sigma(B)/\sigma_m\right)^2\right)}{\sigma_0/\left(1+\left(\sigma_0/\sigma_m\right)^2\right)} \tag{30}$$

When looking at Fig. 4.4.1ab there is a splitting of the peaks in the 3 to 4 T range. This is caused when a maximum in attenuation, Eq. 7, is reached and the center of the peak is where there is a minimum in the 2DEG conductivity [5]. Equation 30, along with Eq. 29, strongly agrees with the experimental results with the parameter $\tau = 5\times10^{-14}$ being found from the experimental data, see Fig. 4.4.1b. This fits the criteria of $\hbar\omega_c < 1$ which is needed to use Eq. 29 in concordance with Eq. 30 [14].

4.5 Gate Pinch Off of Acoustoelectric Current in a Magnetic Field

We now proceeded to generate the DC current throught the use of SAWs. An applied rf power of -10 dBm at a frequency of 840 MHz was applied to the right IDT of the sample, see Fig. 4.3.1; the results can be viewed in Fig. 4.5.1a and the results of a full

magnetic field scan can be viewed in Fig. 4.5.2. It was expected to see a step like behavior in the acoustoelectric current pinch off with quantized steps, similar to what is expected of a standard source-drain bias pinch off [15-16]. What we observed was oscillatory behavior in the measured current. Similar behavior has been observed [17-19] and several accurate descriptions have been formulated [20-21]. These oscillations were attributed to to the subband formation in the QPC. When the one-dimension subband is about to be depopulated, the electron velocity becomes very small, comparable to the sound velocity. In this case the interaction of electrons to the SAW is maximal resulting in the maximum of acoustoelectric current. It should be noted that at the temperature of 4.2 K, the conductance steps are already washed out and cannot be seen in standard transport measurements. However, due to the strong coupling of electrons to the SAW within the suspended nanobridge region, the manifestations of one-dimensional subbands can be seen in the acoustoelectric current.

The wide broadening of the oscillations is due to the higher temperature at which our measurements were taken when compared to narrow oscillations of measurements at lower temperatures [17,22]. The current starts to become negative around -0.65 V at 0 T. The source-drain bias current reaches complete pinch off just below -0.7 V. This behavior seems to be more noticable when the channel length of the QPC is comparable to the SAW wavelength but is still valid for larger wavelengths. In our sample the defined channel length is ~80 nm, compared to other experiments where the channel length is from several hundred nanometers to the order of microns. This narrow channel length

opens the possibility of back scattering [20-21].

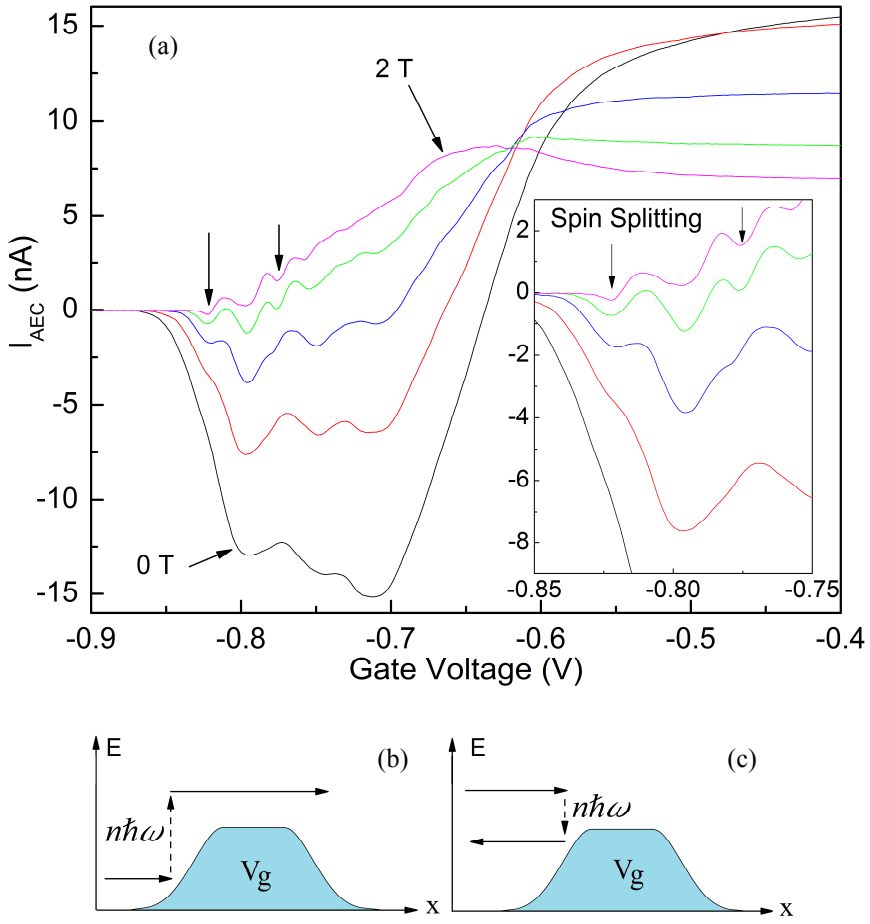

FIG. 4.5.1 (a) Acoustoelectric current at magnetic fields of 0.0, 0.5, 1.0, 1.5, and 2.0 T. Applied rf power of -10 dBm and a frequency of 840 MHz. Inset shows a subset of the data detailing the spin splitting that starts to become visible at 1 T. (b) Inelastic scattering of an electron absorbing n phonon quanta, $\hbar\omega$, allowing it to scatter forward across the QPC gate potential, V_g. (c) Inelastic scattering of an electron emitting n phonon quanta, $\hbar\omega$, causing back scattering from the QPC gate potential, V_g.

From Fig. 4.5.1a the acoustically driven current starts off with a positive

amplitude of 12 to 16 nA but becomes negative due to phonon scattering as the gate voltage decreases. This change in gate voltage changes the effective length of the QPC channel as well as the transmission probabilities for electrons to scatter forward or backward. When the gate voltage is low, or zero, the electrons pass through the channel without any scattering since the potential is low. As the gate potential further decreases the barrier becomes larger causing a small amount of of scattering which reduces the current. Once the gate voltage is decreased to ~-0.65 V the scattering events cause equal transmission in both directions, thus a zero net current. Below this level, -0.65 V, the potential barrier is increased enough to cause the electrons to backscatter; hence, inducing a negative net current until complete pinch off is achieved.

It is accurate to say this is phonon induced since these features do not appear when SAWs are absent, see Fig. 4.1.1. Figs. 4.5.1b and 4.5.1c [20-21] show that the phonon background interacts with the electrons present near the QPC induced potential. This scattering process has low energy, $\hbar\omega << \delta E$, but is largely noticeable since there are n events. The oscillations in the negative region of Fig. 4.5.1a, $I_{AEC} < 0$, occur from non-uniformities in the channel [19]. In *ref. 19* Shilton *et al.* shows that because of non-uniformity in the potential landscape surrounding the QPC there is a change in the channel conductance behavior near pinch off which can cause additional oscillations. This effect can easily be due to slight assymetries that arise during the fabrication process. Another cause can be due to small SAW reflections from the inactive IDT [23] which create small phase shifts causing a spacial modulation of the SAW amplitude.

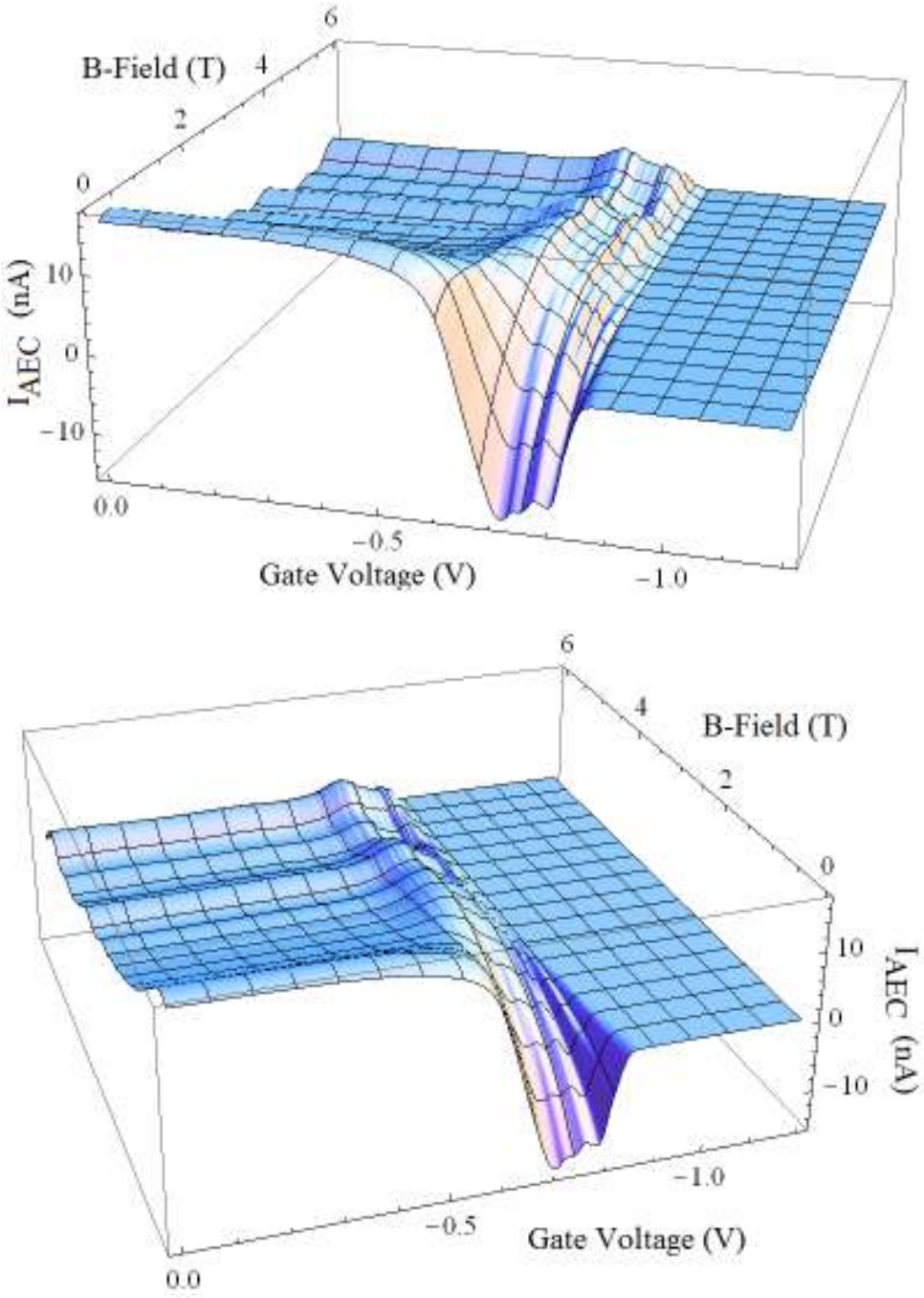

Fig. 4.5.2. 3D plot of pinch off characteristics of the acoustoelectric current under the influence of a perpendicular magnetic field. Gate voltage was applied to the center gate QPC pair. RF power of -10 dBm, 840 MHz, and a 10 μV bias to the source-drain leads.

We were able to achieve strong measurable effects even at high temperature, 4.2 K, due to the suspended QPC. The oscillatory features from pinch off that we have observed fit well with existing theory proving the advantage of a suspended system which allows larger electron-phonon coupling. It was also seen that spin splitting becomes detectable at these higher temperatures. From our results we were able to produce a theoretical model that accurately describes the acoustoelectrically generated current through a 2DEG in the presence of a perpendicular magnetic field. Due to the inherently strong SAW interactions with suspended 2DEGs this system has proven valid for high temperature measurements for future applications.

CHAPTER 5

◄ Additional Measurement Data and Future Work ►

To expand upon some additional work that was done I will present some other findings regarding the devices used. As of yet a proper theory has not been formulated regarding the work in this chapter but will continually be sought after.

5.1 Rectified Acoustoelectric Current

Another device tested showed results of rectified current. This device used the left QPC gate pair as shown in Fig. 2.2.4. The source-drain pinch off exhibited expected results, with the exception of a parallel conduction channel. The complete pinch off required was much larger in magnitude, see Fig. 5.1.1. Along side the source-drain bias of Fig. 5.1.1 is also the acoustoelectric pinch off characteristics. We see that when the SAW is coming from the left of the QPC it generates a different current response when compared to the SAW propagating from the right IDT. The left SAW response exhibits a rectification process that is outlined by Song *et al.* [24]. Here, the propagating potential from the SAW causes a slight modulation in both the source-drain bias and QPC

potential. This small modulation is seen as δV_{QPC} and δV_{SD}. The change in current can then be written in a reduced form as

$$\Delta I \approx \alpha \frac{\partial I}{\partial V_{QPC}} + \beta \frac{\partial^2 I}{\partial V_{QPC}^2} \tag{31}$$

where $\alpha = <\delta V_{QPC}\delta V_{SD}>/V_{SD}$ and $\beta = <\delta V_{QPC}^2>/2$. The two parameters, α and β, are found experimentally.

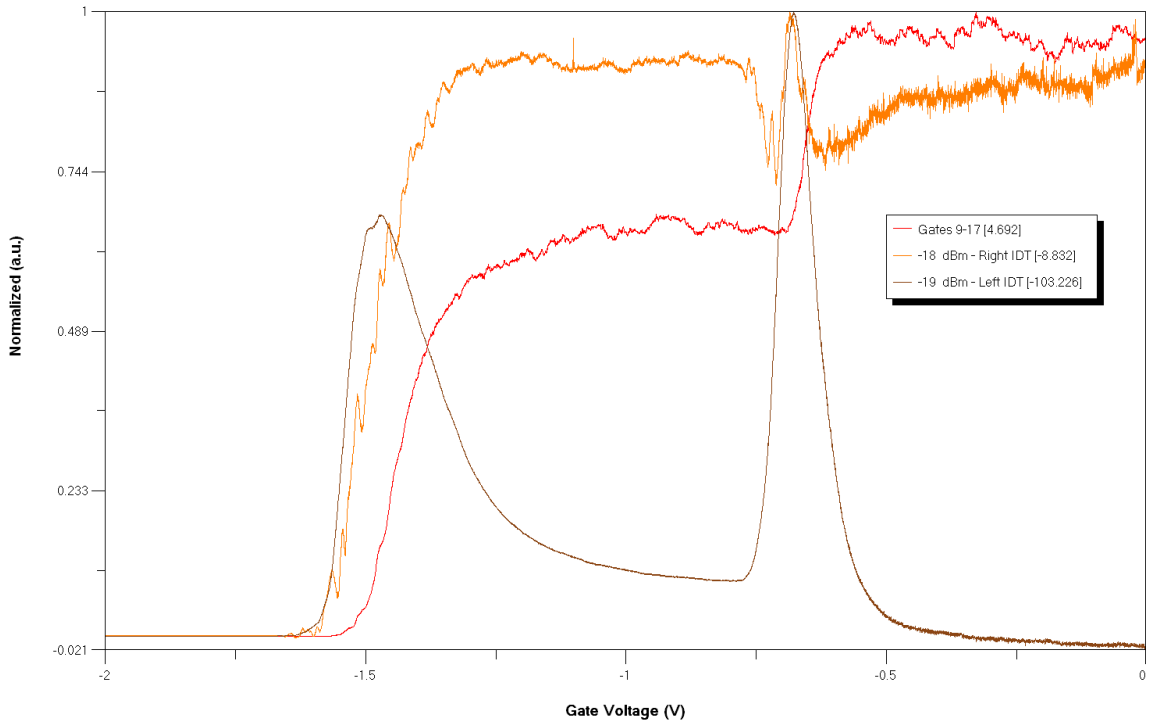

Fig. 5.1.1. Pinch off characteristics of a source-drain bias and acoustoelectric current. The QPC gate used was the left pair, see Fig. 2.2.4. The legend shows the values in which each current trace is normalized to.

From Fig. 5.1.2 it is seen that the derivative of the DC bias from the source-drain matches that of the acoustoelectrically driven current. Since the left QPC pair is used, which is asymmetric, may allow for the reduction of back scattering which could be the explanation of the large forward current in the system. From Fig. 5.1.1 it is seen that the acoustoelectric current magnitude reaches beyond 100 nA when the DC current is in the linear regime.

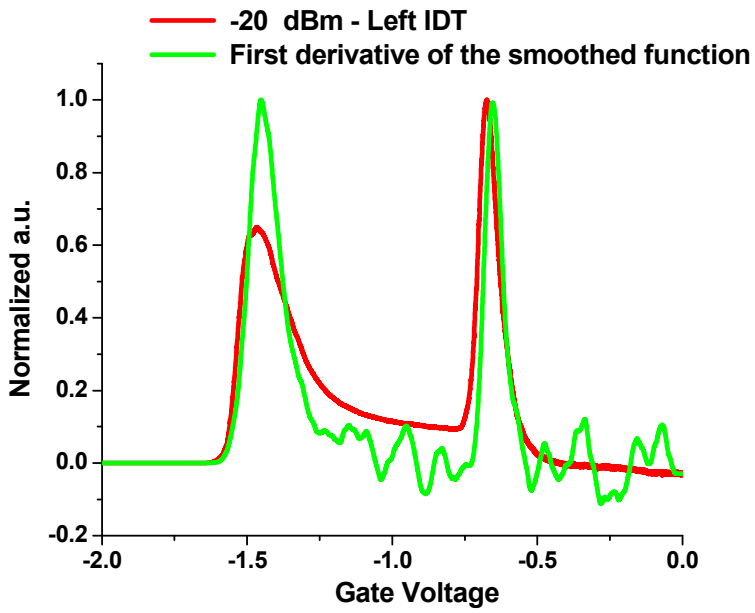

Fig. 5.1.2. Comparison of derivative of the source-drain DC bias with the acoustoelectric current. The match in characteristics indicate a rectification of the current with compliance of Eq. 31.

Again, from Fig. 5.1.1, we see that the SAW from the right IDT creates a different characteristic. Here as the acoustoelectric current approaches pinch off there are slight oscillations which match up with the DC bias “steps” in the current profile [19]. This

behavior has a similar theoretical background to what is discussed in section 4.5. The loss of symmetry gives us a different result here.

5.2 Phase Locked Acoustoelectric Current Pinch Off

Another set of tests performed involves supplying an rf signal to both IDTs, the left and right, and changing the phase between the two signals [22]. As the phase is changed the gate voltage is swept on the QPC gates, the results can be seen in Fig. 5.2.1 and Fig 5.2.2. When viewing these two figures it is best to look back at Fig. 5.1.1 to match up the gate voltage range as to identify the features of the two figures, Fig. 5.2.1-5.2.2. In Fig. 5.2.1 the data is a subset of Fig. 5.1.1 in the gate voltage range of -1.2 to -1.7 V. With in this range complete pinch off of the acoustoelectric current is achieved, as can also be seen from Fig. 5.2.2. The oscillation near pinch off in Fig. 5.2.1ab are easily seen and even more pronounced, the details of this are discussed in section 4.5. As we sweep the phase of the two locked signals this further increases the spatial modulation of the SAW as it moves through the QPC. These effects again manifest themselves here differently then what is shown in Fig. 5.2.2. Again, since this region is beyond the DC pinch off regime it is purely an amplitude modulation due to the shift in the potential landscape [19].

The results shown in Fig. 5.2.2 correspond to a different region. Here, the voltage range is from -0.5 to -0.8 VDC, refer to Fig. 5.1.1 for the DC reference. In this region the

QPC has not yet reached complete pinch off, but a parallel conductance channel is believed to exist (due to material differences) that becomes pinched off. This leads to the behavior shown in Fig. 5.2.2 with the added feature of not only having the spatial modulation but also the electron phonon interaction as described in section 4.5. This is further evidence for the verification of the theory presented earlier.

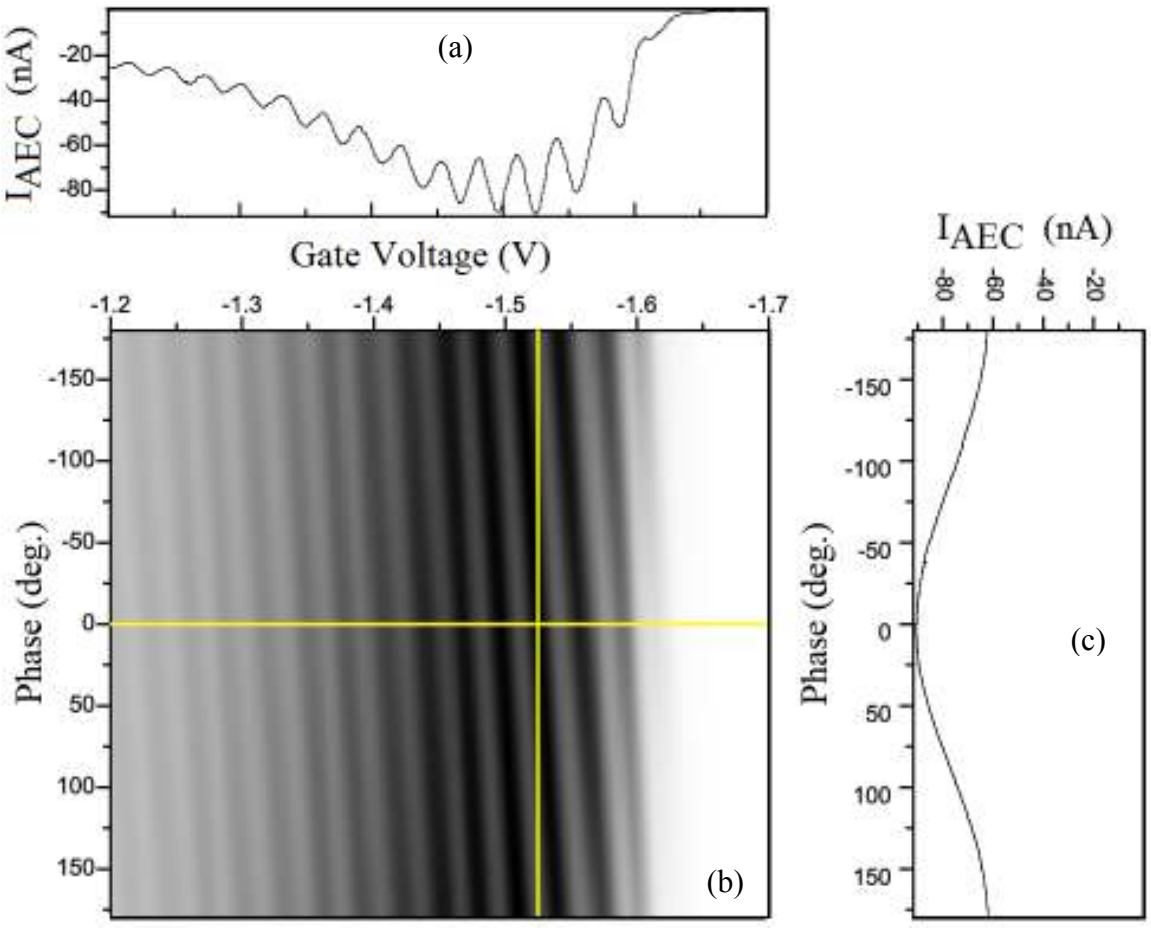

Fig. 5.2.1. Acoustoelectric phase pinch off profile for an applied rf signal of f = 1.488 GHz and applied power of -19 and -18 dBm to the left and right IDTs, respectively. (a) Acoustoelectric Current vs. Gate

Voltage at a 0° phase difference. (b) Density plot of acoustoelectric current of Phase vs. Gate Voltage. (c) Current vs. Phase with a constant gate voltage of -1.525 V. Refer to Fig. 5.1.1 for gate voltage range.

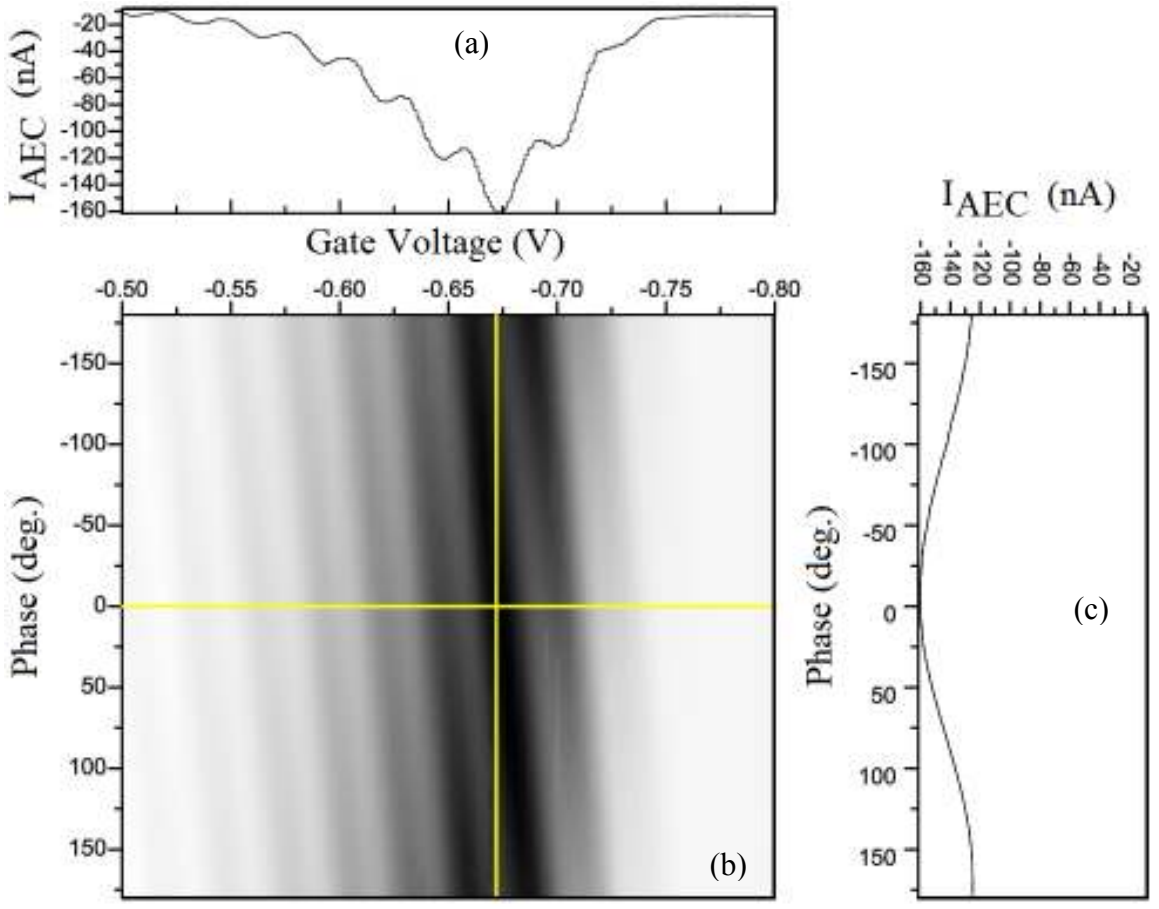

Fig. 5.2.2. Acoustoelectric phase pinch off profile for an applied rf signal of f = 1.488 GHz and applied power of -19 and -18 dBm to the left and right IDTs, respectively. (a) Acoustoelectric Current vs. Gate Voltage at a 0° phase difference. (b) Density plot of acoustoelectric current of Phase vs. Gate Voltage. (c) Current vs. Phase with a constant gate voltage of -1.525 V. Refer to Fig. 5.1.1 for gate voltage range.

5.3 Variation of σ_M

In our findings we are lead to believe that the constant, σ_m, may actually not be a constant at all and may possibly depend on the geometric boundaries of the device as well as electronic properties such as edge channel effects. Currently all research thus far uses this value as a constant, but in every use of the value the experimenter is left to determine the value σ_m through analysis of the data given. The value is reported as given by the equation

$$\sigma_m = v_s(\varepsilon_{GaAs} + \varepsilon_0) \tag{32}$$

In our findings, as a result of trying to develop a new theory, have so far lead us to believe that there is more to this. We first started by trying to expand upon the theory in section 4.5 and use Eq. 29 as a basis along with Eq. 30. For low field values we were able to achieve a workable theory that seemed to be on the right track but is not yet complete in the time of writing this thesis.

The current normalized to its value at the zero magnetic field and zero gate voltage is given by

$$\frac{J(V_g,B)}{J(0,0)} = \frac{\sigma(V_g,B)\Big/\left(1+\left(\sigma(V_g,B)/\sigma_m\right)^2\right)}{\sigma_0\Big/\left(1+\left(\sigma_0/\sigma_m\right)^2\right)} \tag{33}$$

where $\sigma(V_g,B) = \sigma(B)\sigma^{exp}(V_g)$. From here, $\sigma^{exp}(V_g)$ is reduced to $\sigma^{exp}(V_g) = I(V_g)/I(0)$, where $I(V_g)$ is the source-drain bias current and is normalized with $I(0)$. We use Eq. 33 to determine σ_m since the left side of Eq. 33 was taken from experiment and gives

$$\sigma_m(V_g,B) = \sigma(V_g,B)\left(\frac{\sigma(V_g,B)}{\sigma(0,0)}\frac{J(0,0)}{J(V_g,B)}\left(1+\frac{\sigma^2(0,0)}{\sigma_m^2(0,0)}\right)-1\right)^{-1/2} \qquad (34)$$

Equation 34 is plotted below, Fig. 5.3.1, for $\tau = 10^{-13}$ s, T = 4.2 K, $n_e = 4.2\cdot10^{15}$ m^{-2}, and $\sigma_m(0,0) = 4\cdot10^{-7}$ $(\Omega/\text{sq})^{-1}$ [6]. Of course, substitution of this function back to Eq. 33 completely reproduces the experimental current. However, this function does not have valid values for the gate voltage smaller than -0.7, because in this case the expression under the square-root of Eq. 33 is negative. The same is true for the small region of the figure above at magnetic fields smaller than 1 T and the gate voltage smaller than -0.65. Most probably, in these regions Eq. 33 does not work because of additional effects. I believe that particular reason is that the QPC current (shown in the first figure of these notes) is affected by the nanobridge vibrations even without SAW.

As of now this theory is still being worked on and is of great interest. So far we have a good foundation to move forward on and work will be continued even beyond the submission of this article and after graduation.

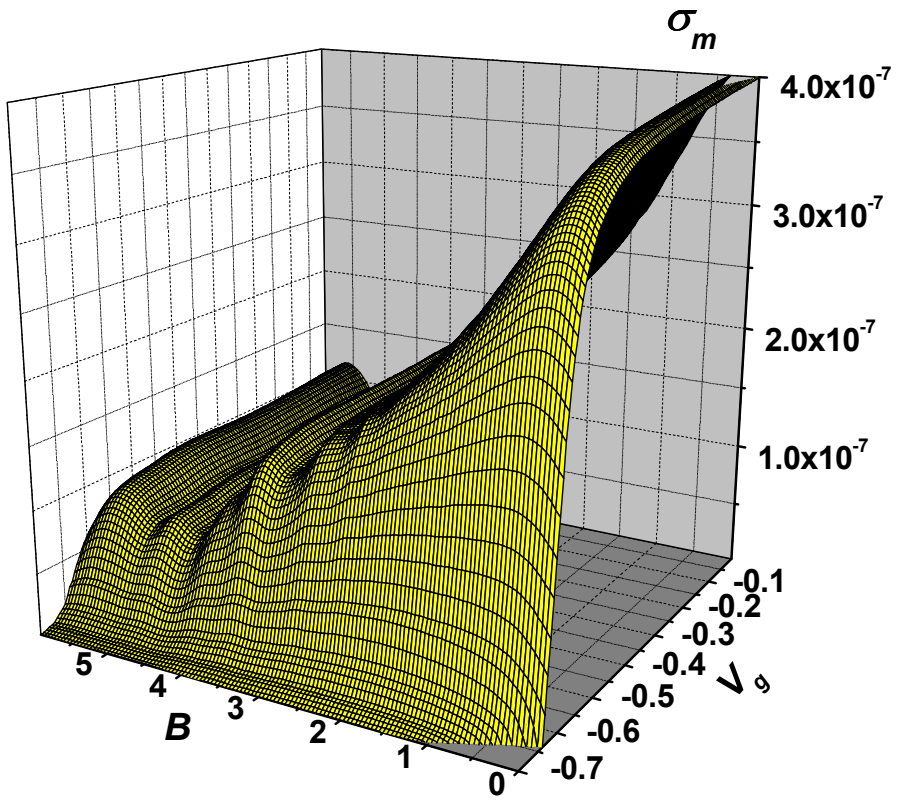

Fig. 5.3.1. Theoretical value of σ_m which is believed to be a constant. This data, once substituted back into the original theory, can reproduce the experimental results of Fig. 4.5.1 and Fig. 4.5.2 at various fields.

Appendix A – Acoustic Waveguide Source Code

The following code was written in Microsoft Notepad and was executed as a macro in DesignCAD 2000 LT to generate the required DC2 file. The newly generated DC2 file was then loaded and executed with NPGS to e-beam write the pattern onto the sample. This code is free to use without copyright and is free to distribute.

```
'This program will create an etch window opening shaped to an
exponential acoustic
'horn. This is used as a waveguide for SAWs. Edit the Horn Parameters
as needed to
'match the desired feature of the acoustic horn.
'
'Written by: Dustin J. Kreft
'Date: 1-18-10
'
'========= Update History ========================================
'
'Initials        Date         Description
'--------        --------     -----------
'DJK              1-25-10     Extended etch area to larger electrodes
'DJK              8-20-10     Changed several 'Horn Parameter' values


'========= Setup/System Parameters ================================
SYS(4) = 1                    'Set line type to dash
SYS(1) = 0                    'Clear all set points
SYS(80) = 0                   'Clear any selected points
SYS(41) = 1                   'Turn on rubber band
SYS(6) = 0                    'Line width

'========= Horn Parameters ========================================
sXCenter = 0.0
sYCenter = 0.0

sXStart = 0.0
sXEnd = 14          ' 14 um
sXIncrement = 0.1   ' 0.1 um (100 nm)
sXTube = 6          ' Tube Length, 6 um

sVelocity = 1600*10^6    'um / second
Pi = 3.14159
sFreqCutOff = 25*10^6    'Cut off frequency (Hz)

sA = 2.0            ' A*Exp[m*x] 2.0 um
sm = 0.0            ' A*Exp[m*x]
sVal = 0.0          ' sVal = A*( Exp[m*x] )^2

sm = (2*Pi*sFreqCutOff) / sVelocity
```

```
sEtchGap = 0.3     'Spacing for etch gap of horn, 0.3 um

sTemp = 2*sXEnd + sXTube

strTemp$ = SYS$(42)      ' Save default window text
SYS$(42) = "Acoustic Waveguide"

'LINE #49

'========= Window ========================================================
WINDOW 12, 50
PRINT " This will generate an exponential curve fitting a horn"
PRINT ""
PRINT " Parameters:"
PRECISION 0
PRINT " - Wet/Dry Etch Gap = ", sEtchGap * 1000, " nm"
PRINT " - Data Point Spacing = ", sXIncrement*1000, " nm"
PRECISION 3
PRINT " - Frequency Cutoff = ", sFreqCutOff / 10^6, " MHz"
PRINT " - Total Horn Width = ", sTemp, " um"
PRINT " - Throat Gap = ", sA, " um"
PRECISION 0
PRINT " - Total Data Points Per Entity ~ ", (sXEnd-sXStart)/sXIncrement
* 4 + 5
PRINT ""
COLOR 3,0
Print " Press any key to continue... "
COLOR 2,0
PRINT " Dustin J. Kreft ©"
ANYKEY
WCLOSE

PRECISION 3

'Assume version 9 or greater
nMaxPoints = 1000

'LINE #78

'========= Large Electrode Parameters ==============================
sSlope = 0.6522          'Slope of electrode line closest to (0,0), um
sYInt = 3.097            'Y-Intercept of electrode line, um

'========= Generate Upper Curve ====================================

sYCenter = -sA/2

'LINE #88

>LINE
{
```

```
 'Create the negative x portion of the horn
 FOR J = -sXEnd TO sXStart STEP sXIncrement
      sVal = sA*(EXP(-sm*J))^2
      <PointXYZ [ J + sXCenter - sXTube/2, sVal + sYCenter, 0.0000 ]
 NEXT J

 'Continue and create the positive portion of the horn
 FOR J = sXStart TO sXEnd STEP sXIncrement
      sVal = sA*(EXP(sm*J))^2
      <PointXYZ [ J + sXCenter + sXTube/2, sVal + sYCenter, 0.0000 ]
 NEXT J

 'Move up and create the positive end of the horn, and sweep backward
 FOR J = sXEnd TO sXStart STEP -sXIncrement
      sVal = sA*(EXP(sm*J))^2
      <PointXYZ [ J + sXCenter + sXTube/2 - sEtchGap, sVal + sYCenter +
sEtchGap, 0.0000 ]
 NEXT J


 'Create negative end
 FOR J = sXStart TO -sXEnd STEP -sXIncrement
      sVal = sA*(EXP(-sm*J))^2
      <PointXYZ [ J + sXCenter - sXTube/2 + sEtchGap, sVal + sYCenter +
sEtchGap, 0.0000 ]
 NEXT J

 'Close the structure
 <PointXYZ [ J + sXCenter - sXTube/2, sA*(EXP(-sm*(-sXEnd)))^2 +
sYCenter, 0.0000 ]

}

SYS(41) = 0       'Turn off rubber band

'========= Generate Lower Curve ====================================

SYS(1) = 0                    'Clear all set points
SYS(80) = 0                   'Clear any selected points
SYS(41) = 1                   'Turn on rubber band

>LINE
{

 'Create the negative x portion of the horn
 FOR J = -sXEnd TO sXStart STEP sXIncrement
      sVal = sA*(EXP(-sm*J))^2
      <PointXYZ [ J + sXCenter - sXTube/2, -sVal - sYCenter, 0.0000 ]
 NEXT J
```

```
 'Continue and create the positive portion of the horn
 FOR J = sXStart TO sXEnd STEP sXIncrement
      sVal = sA*(EXP(sm*J))^2
      <PointXYZ [ J + sXCenter + sXTube/2, -sVal - sYCenter, 0.0000 ]
 NEXT J


 'Move up and create the positive end of the horn, and sweep backward
 FOR J = (sXEnd-sEtchGap) TO sXStart STEP -sXIncrement
      sVal = sA*(EXP(sm*J))^2
      <PointXYZ [ J + sXCenter + sXTube/2 - sEtchGap, -sVal - sYCenter
- sEtchGap, 0.0000 ]
 NEXT J

 'Create negative end
 FOR J = sXStart TO (-sXEnd+sEtchGap) STEP -sXIncrement
      sVal = sA*(EXP(-sm*J))^2
      <PointXYZ [ J + sXCenter - sXTube/2 + sEtchGap, -sVal - sYCenter
- sEtchGap, 0.0000 ]
 NEXT J

 'Close the structure
 <PointXYZ [ -sXEnd + sXCenter - sXTube/2, -sA*(EXP(-sm*(-sXEnd)))^2 -
sYCenter, 0.0000 ]

}

SYS(41) = 0        'Turn off rubber band

WINDOW 7, 35
COLOR 3,0
PRINT "              FINISHED!               "
COLOR 1,0
Print ""
PRINT " Be sure to change the writing order  "
PRINT " and writing direction for each entity."
PRINT ""
COLOR 3,0
PRINT " Press any key to continue "
PRINT ""
ANYKEY
WCLOSE

SYS$(42) = strTemp$      'Set window string back to default

END                'End of program
```

Appendix B – Custom Measurement Software

To perform the measurements and collect data I developed custom software, from the ground up, to achieve this task. This project was taken on because of some of the pitfalls and shortcomings of available software. This software was developed in both Microsoft Visual Basic and C/C++ and was developed along side the insert, section 3.1, used for measurements. The software works by communicating over the GPIB bus and gathering data from the instruments as instructed by the custom scripting language developed by me. The scripting language is quite similar to BASIC with a few added commands to do real time plotting and GPIB communications.

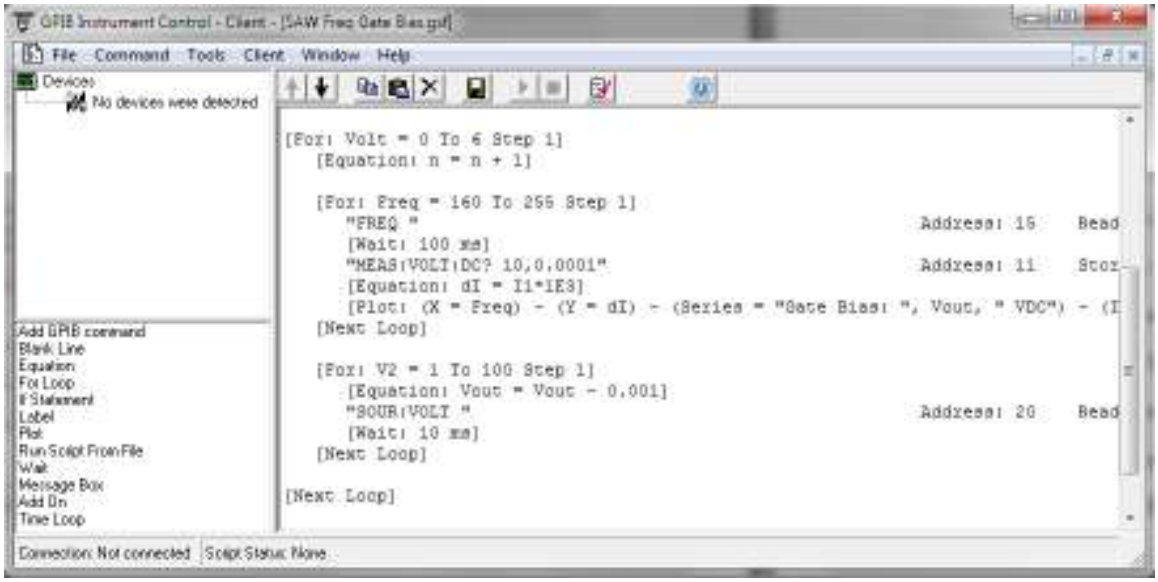

Fig. B.1. Screenshot of custom measurement software showing a portion of a script that controls measurement I/O.

A sample script is shown in Fig. B.1 which highlights some of the syntax of the custom scripting language developed. As the script executes it gathers data from the instruments and shows them in a real time plot, see Fig. B.2. The software also has added features of post processing such as several built in math functions and drawing objects for graphic output.

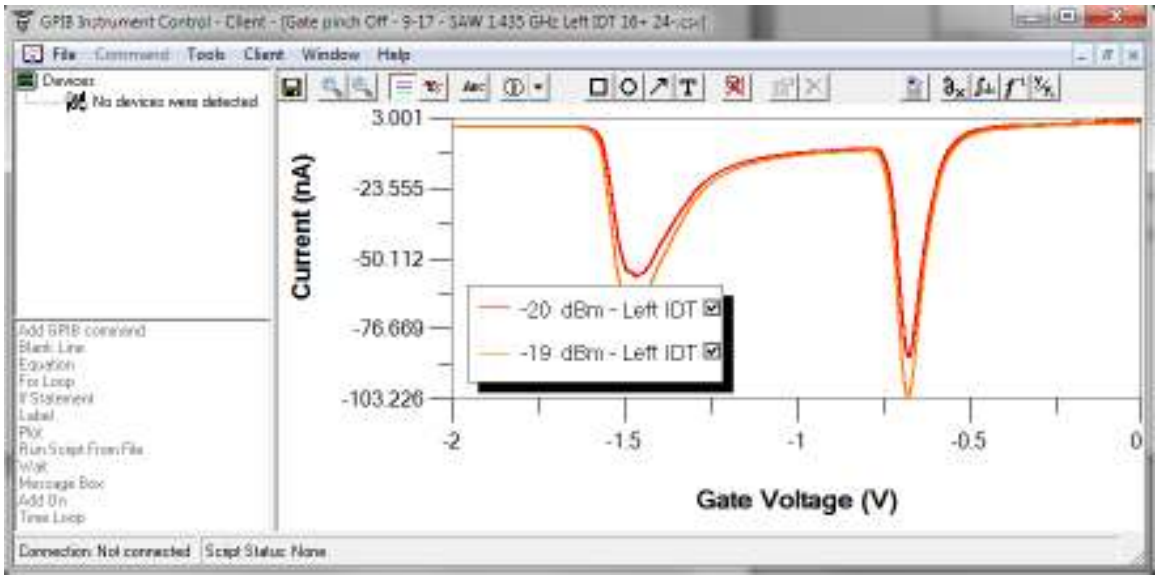

Fig. B.2. Screenshot of custom software showing the data plot that updates in real time as data is being gathered from the instruments on the GPIB bus.

This software has proved to be quite valuable in my research, as well as to others, and offers the desired features needed to quickly design a measurement algorithm and collect the data. Not all of the software's features are listed but in developing this I was able to create a highly customizable program that fits any measurement need.

Appendix C – PMN-PT Project

Another project in which I was involved in was the development of devices using a thin film PMN-PT material which was developed by S.H. Baek who was a student of C.B. Eom here at UW-Madison in the Department of Material Science and Engineering. All work presented here in Appendix C is from [25]. In this work a new thin film PMN-PT material was grown which exhibits stronger piezoelectric effects than commercial PMN-PT and PZT. This new material has a transverse piezoelectric coefficient of $e_{31} \approx 27.5$ C/m^2, which is a large improvement compared to the latest available material of gradient-free PZT which has a coefficient of $e_{31} \approx 17.5$ C/m^2.

The material consists of a 300 nm PMN-PT film grown on Si with a 200 nm $SrRuO_3/SrTiO_3$ buffer layer to account for lattice mismatch between the Si and PMN-PT as well as offer a backside electrode. The device made out of the PMN-PT material for testing was a cantilever 34 μm in length, see Fig. C.1a. Testing was done using a white light interferometer to detect the cantilever displacement as a function of applied DC voltage, see Fig. C.1b. The results show the advantages of this material in that the cantilever requires a smaller voltage/power to actuate the device. In Fig. C.1d we see the tip displacement of the cantilever responds much more readily when compared to a typical electrostatic cantilever, thus making devices of this new PMN-PT material ideal for low energy applications and energy harvesting systems.

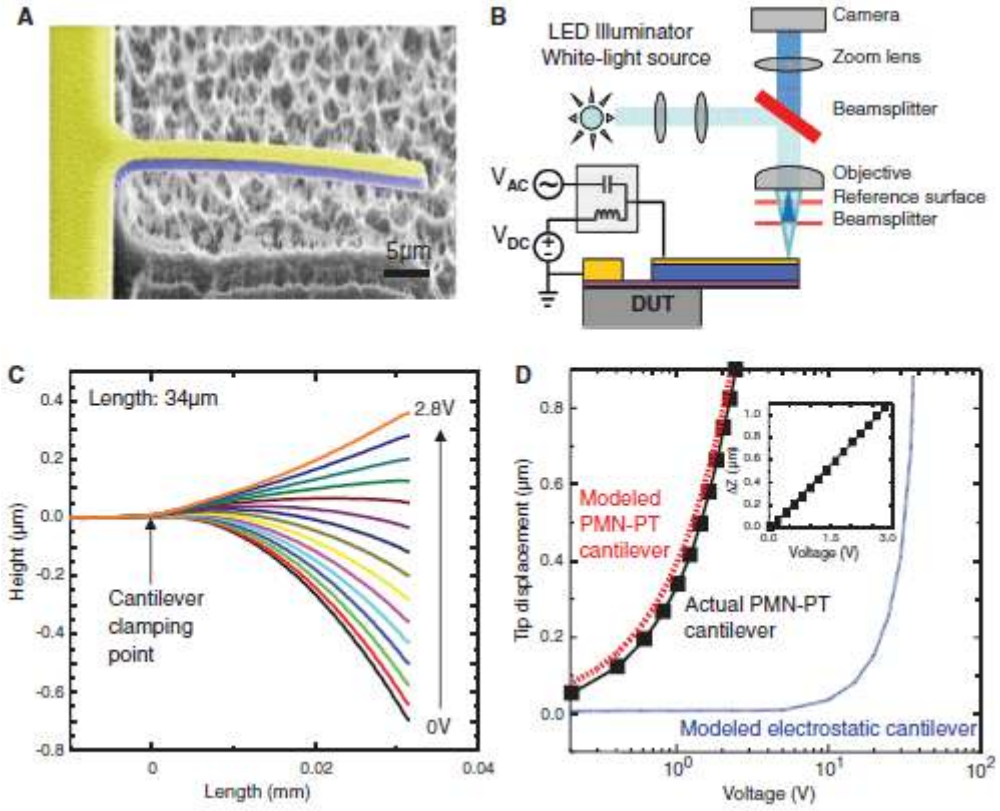

Fig. C.1. Fabrication and characterization of PMN-PT microcantilevers. (A) SEM image of a PMN-PT cantilever. (B) Schematic illustration of the measurement set-up. Both dc and ac fields can be applied between the top and bottom electrodes. LED, light-emitting diode; DUT, device under test. (C) PMN-PT cantilever profile as a function of dc voltage. (D) Tip displacement of the 34-mm-long cantilever versus applied dc voltage. (Inset) Linear scale of tip displacement. The dotted red line denotes the simulation result for a PMN-PT cantilever with the same geometry. The blue dotted line represents the modeled result for an electrostatic cantilever with comparable geometry. ΔZ is the tip displacement.

Bibliography

[1] C. Campbell, *Surface Acoustic Wave Devices for Mobile and Wireless Communications*, Academic Press, Inc, 1998, ISBN 0-12-157340-0, San Diego, CA, USA.

[2] D.J. Kreft and R.H. Blick, *Surface Acoustic Waves and Nano-Electromechanical Systems, Acoustic Waves – From Microdevices to Helioseismology*, M.G. Beghi (Ed.), 2011, ISBN: 978-953-307-572-3, InTech

[3] M. Kataoka *et al*., Phys. Rev. Lett. **98**, 46801 (2007).

[4] C. Rocke *et al.*, Phys. Rev. Lett. **78**, 4099 (1997).

[5] A. Wixforth *et al.*, Phys. Rev. B **40**, 7874 (1989).

[6] A. Wixforth, J. P. Kotthaus, and G. Weimann, Phys. Rev. Lett. **56**, 2104 (1986).

[7] C.C.W. Ruppel and T.A. Fjeldy, *Advances in Surface Acoustic Wave Technology, Systems and Applications, Volume 2*, 2001, ISBN: 981-02-4538-6, World Scientific Publishing Co. Pte. Ltd.

[8] B.J. van Wees *at al.*, Phys. Rev. Lett. **60**, 848 (1988).

[9] D.A. Wharam *et al.*, J. Phys. C **21**, L209 (1988).

[10] M. Buttiker, Phys. Rev. B **41**, 7906 (1990).

[11] V. Salmon, JASA **17**, 212 (1946).

[12] H. Ibach and H. Luth, *Solid-State Physics: An Introduction to Principles of Materials Science*, 2009, ISBN: 978-3-540-93803-3, Springer Publishing

[13] M. Kuok *et al*., Journ. Appl. Phys. **89**, 12 (2001)

[14] T. Ando *et al.*, Rev. Mod. Phys. **54**, 437 (1982).

[15] V.I. Talyanskii *et al.*, Phys. Rev. B **62**, 8410 (2000).

[16] L. Song *et al.*, Solid State Comm. **150**, 292 (2010).

[17] J.M. Shilton *et al.*, J. Phys.:Condens. Matt. **8**, L337 (1996).

[18] F.J. Ahlers *et al.*, Current Applied Phys. **4**, 529 (2004).

[19] J.M. Shilton *et al.*, J. Phys.: Condens. Matt. **8**, L531 (1996).

[20] F.A. Maao and Y. Galperin, Phys. Rev. B **56**, 4028 (1997).

[21] H. Totland *et al.*, Phys. Rev. B **56**, 15299 (1997).

[22] F.W. Beil *et al*., Phys. Rev. Lett. **100**, 026801 (2008).

[23] M.R. Astley *et al.*, Appl. Phys. Lett. **89**, 132102 (2006).

[24] J. Song *et al.*, Appl. Phys. Lett. **92**, 223115 (2008).

[25] S.H. Baek *et al.*, Science **334**, 598 (2011).